# Global high-resolution mapping of ocean circulation from TOPEX/Poseidon and ERS-1 and -2

N. Ducet, Pierre-Yves Le Traon, Gilles Reverdin

JOURNAL OF GEOPHYSICAL RESEARCH, VOL. 105, NO. C8, PAGES 19,477–19,498, AUGUST 15, 2000

# Global high-resolution mapping of ocean circulation from TOPEX/Poseidon and ERS-1 and -2

N. Ducet and P. Y. Le Traon
Space Oceanography Division, CLS, Ramonville Saint-Agne, France

G. Reverdin
Laboratoire d'Etudes en Géophysique et Océanographie Spatiales, Toulouse, France

**Abstract.** This study focuses on the improved estimation of mesoscale surface ocean circulation obtained by merging TOPEX/Poseidon (T/P) and ERS-1 and -2 altimeter measurements between October 1992 and May 1998. Once carefully intercalibrated and homogenized, these data are merged through an advanced global objective analysis method that allows us to correct for residual long wavelength errors and uses realistic correlation scales of ocean dynamics. The high-resolution (0.25° × 0.25°) merged T/P + ERS-1 and -2 sea level anomaly maps provide more homogeneous and reduced mapping errors than either individual data set and more realistic sea level and geostrophic velocity statistics than T/P data alone. Furthermore, the merged T/P + ERS-1 and -2 maps yield eddy kinetic energy (EKE) levels 30% higher than maps of T/P alone. They also permit realistic global estimates of east and north components of EKE and their seasonal variations, to study EKE sources better. A comparison of velocity statistics with World Ocean Circulation Experiment surface drifters in the North Atlantic shows very good agreement. Comparison with contemporary current meter data in various oceanic regimes also produces comparable levels of energy and similar ratios of northward and eastward energy, showing that the maps are suitable to studying anisotropy. The T/P + ERS zonal and meridional components of the mapped currents usually present comparable rms variability, even though the variability in the Atlantic is more isotropic than that in the Pacific, which exhibits strong zonal changes. The EKE map presents a very detailed description, presumably never before achieved at a global scale. Pronounced seasonal changes of the EKE are found in many regions, notably the northeastern Pacific, the northeastern and northwestern Atlantic, the tropical oceans, and the zonally extended bands centered near 20°S in the Indian and western Pacific Oceans and at 20°N in the northwestern Pacific.

## 1. Introduction

It is now generally admitted that at least two altimetric missions are needed to resolve the main space scales and timescales of the ocean circulation, in particular, the mesoscale [e.g., *Koblinsky et al.*, 1992; *Blayo et al.*, 1997; *Le Traon and Dibarboure*, 1999, hereinafter referred to as LD99]. LD99 have analyzed, in particular, the mesoscale mapping capabilities of multiple altimeter missions. They show that existing and future two-satellite configurations (T/P and ERS and, later on, Jason-1 and Envisat) will provide rather good mapping of SLA mesoscale variability (mapping error below 10% of the signal variance). On the other hand, *Greenslade et al.* [1997] concluded that the mesoscale variability cannot be mapped with acceptable accuracy with any of the existing or future two- or three-satellite configurations. *Greenslade et al.* [1997] required, however, a very homogenous mapping error. Although the mesocale mapping errors are not homogenous, LD99 argue that they remain sufficiently small relative to the signal. The combination of TOPEX/Poseidon (T/P) and ERS-1 and -2, and later on, Envisat and Jason-1, should thus allow a mapping of sea level and ocean circulation variations with good accuracy.

However, merging multisatellite data sets is not an easy task. It first requires homogeneous and intercalibrated sea surface height (SSH) data sets. It is then necessary to extract consistent sea level anomaly (SLA) data from the different satellites. Finally, advanced interpolation techniques are needed to map SLA data onto a regular space/time grid. Gridded SLA data can be considered as a final merged product; they can be used directly for signal analysis and in comparison with numerical models and in situ measurements [e.g., *Chao and Fu*, 1995; *Hernandez et al.*, 1995]. They may also be assimilated into ocean circulation models since they provide both data and associated error estimates at each grid point, although the assimilation of along-track data may be preferred for sophisticated assimilation schemes [*Fukumori*, 1995].

Effective merging techniques have been developed at CLS Space Oceanography Division. It has been shown that homogenous and intercalibrated SSH data sets can be obtained by using the most precise mission (T/P and, later on, Jason-1) as a reference for the less precise missions [*Le Traon et al.*, 1995; *Le Traon and Ogor*, 1998]. F. Hernandez (manuscript in preparation, 1999) has also proposed a method to get consistent mean profiles for the T/P and ERS missions and *Le Traon et al.*



Paper number 2000JC900063.
0148-0227/00/2000JC900063$09.00

[1998] have developed an improved mapping technique for multiple altimeter missions. Such new merging techniques now allow us to derive combined SLA maps from T/P and ERS with high accuracy and resolution. In this paper we show the first results of the global mapping of sea level and ocean circulation variations from T/P, used separately or combined with ERS-1 and -2, over a five and a half year period. Rather than solving a particular oceanographic issue, the main objective of this work is to demonstrate the effectiveness and accuracy of the merging technique and its contribution to mesoscale ocean circulation studies.

The paper is organized as follows. The data, data processing, and objective analysis method are presented in section 2. The comparison of T/P and ERS mapped data is discussed in section 3. The contribution of the merging of the two data sets is analyzed in section 4. A careful validation of the combined T/P + ERS product by comparing the velocity statistics with the ones from drifters and near-surface current meters is done in section 5. Features in the combined mapped data are presented, focusing on eddy kinetic energy (EKE) seasonal variations, in section 6.

## 2. Mapping Methodology

### 2.1. Data and Data Preprocessing

We use five and a half years of T/P reprocessed Merged Geophysical Data Records (GDRs) (GDR-M Version C), distributed by *Archiving, Validation, and Interpretation of Satellite Oceanographic Data* (*AVISO*) [1996], and of ERS-1 and -2 Ocean Products (OPRs), distributed by *Centre ERS d'Archivage et de Traitement* (*CERSAT*) [1994, 1996]. The data span the period from the beginning of October 1992 to the end of April 1998. This corresponds to 207 full 10 day repeat cycles (from cycle 2 to 208) for T/P but only to 4 years and 5 months of ERS 35 day repeat cycle mission data (ERS-1 phases C and G plus ERS-2 phase A). The missing ERS-1 period corresponds to the 168 day repeat cycle geodetic mission (phases E and F) from December 24, 1993, to March 24, 1995. When necessary, ERS altimetric corrections were updated to make T/P and ERS corrections homogeneous. For example, the CSR3.0 tidal model was used for both missions. The dry tropospheric and inverse barometer corrections, which are derived from the French meteorological model Action de Recherche Petite Echelle Grande Echelle (ARPEGE) [*Decque et al.*, 1994] (until the end of the ERS-1 geodetic mission), were also replaced by corrections derived from the European Center for Medium-Range Weather Forecasts (ECMWF) model, consistent with the ones for T/P. For more details on the corrections applied to T/P and ERS-1/2 SSH data the reader is referred to *Le Traon and Ogor* [1998].

Merging multiple altimeter missions requires first homogeneous and intercalibrated SSH data sets. Intercalibrated data sets are obtained by performing a global crossover adjustment of ERS orbit, using the more precise T/P data as a reference [*Le Traon and Ogor*, 1998]. Since geoids are not known at small spatial scales with a sufficient accuracy, data along each satellite track need to be referenced to a mean profile, using a repeat track analysis, to get along-track SLAs. The T/P mean profile was calculated from the first three complete years of T/P along-track data (January 1993 to December 1995). Because of the gap due to the geodetic mission and its longer repeat track period, an ERS mean profile computed over the same period would not be compatible with the T/P mean and would be less precise. To reduce the contamination of ocean signal variability on the ERS mean and to get a consistent mean for the T/P and ERS missions, T/P SLA data are thus used to correct ERS SSH along-track data prior to the computation of the ERS mean profile (F. Hernandez, manuscript in preparation, 1999). For each ERS cycle, T/P SLA data are interpolated along ERS tracks using an optimal interpolation method similar to the one described in section 2.2 and then subtracted from the ERS SSH data. This allows us to remove the large-scale ocean signal variability in the ERS data (e.g., seasonal steric height signal), which otherwise, because of inadequate time sampling, would be aliased onto the ERS mean.

To reduce measurement noise and mapping computer time, the SLA files are filtered (using a linear Lanczos [*Hamming*, 1977] low-pass filter) and subsampled. The Lanczos filter cutoff wavelength depends on latitude, taking into account variations in the typical spatial scales of the ocean signal: 300 km equatorward of 10°N/°S, 200 km between 10° and 30°N/°S, 100 km between 30° and 50°N/°S, and 70 km above 50°N/°S. Filtering considerably reduces the instrumental noise. The data are then subsampled according to the degree of smoothing: one point in seven from the equator to 10°N/°S (roughly every 50 km), one point in five from 10° to 30°N/°S (roughly every 35 km), and one point in three poleward of 30°N/°S (roughly every 21 km) are kept as final along-track observations.

### 2.2. Mapping

The main characteristics of the mapping method are given here; for a more detailed description, see *Le Traon et al.* [1998]. The theoretical formulation of the estimator and the associated mapping error, along with more details on the data selection are given in the appendix. The method is a global suboptimal space/time objective analysis that takes into account along-track correlated errors. For each grid point, data are initially selected in a large subdomain, whose radius is 3 times larger than the space correlation scales (varying with latitude, see below). As the data selected in the large domain are not centered, a mean is removed before the analysis, and added back afterward. This mean corresponds to the average of the data weighted by the inverse of the long wavelength error variance (different for each satellite). Next, data are selected for the objective mapping: inside a subdomain within roughly the zero-crossing of the space correlation scale, all data are retained; outside this subdomain, only one point out of four is retained. These latter observations are used to correct for long wavelength errors, enabling us to separate long wavelength errors from the ocean signal.

The space correlation scales (zero crossing of the correlation function) are set as follows [see also *Oschlies and Willebrand*, 1996]:

$14° < \text{Latitude} < 14°$

$$\text{meridional} = 250 \text{ km}$$

$$\text{zonal} = 50 + 300\left(\frac{900}{2\ \text{Lat}^2 + 900}\right) \text{ km}$$

Poleward of 14°

$$\text{meridional} = \text{zonal} = 50 + 250\left(\frac{900}{\text{Lat}^2 + 900}\right) \text{ km},$$

where Lat stands for latitude (in degrees).

These scales are intended to represent typical space scales of

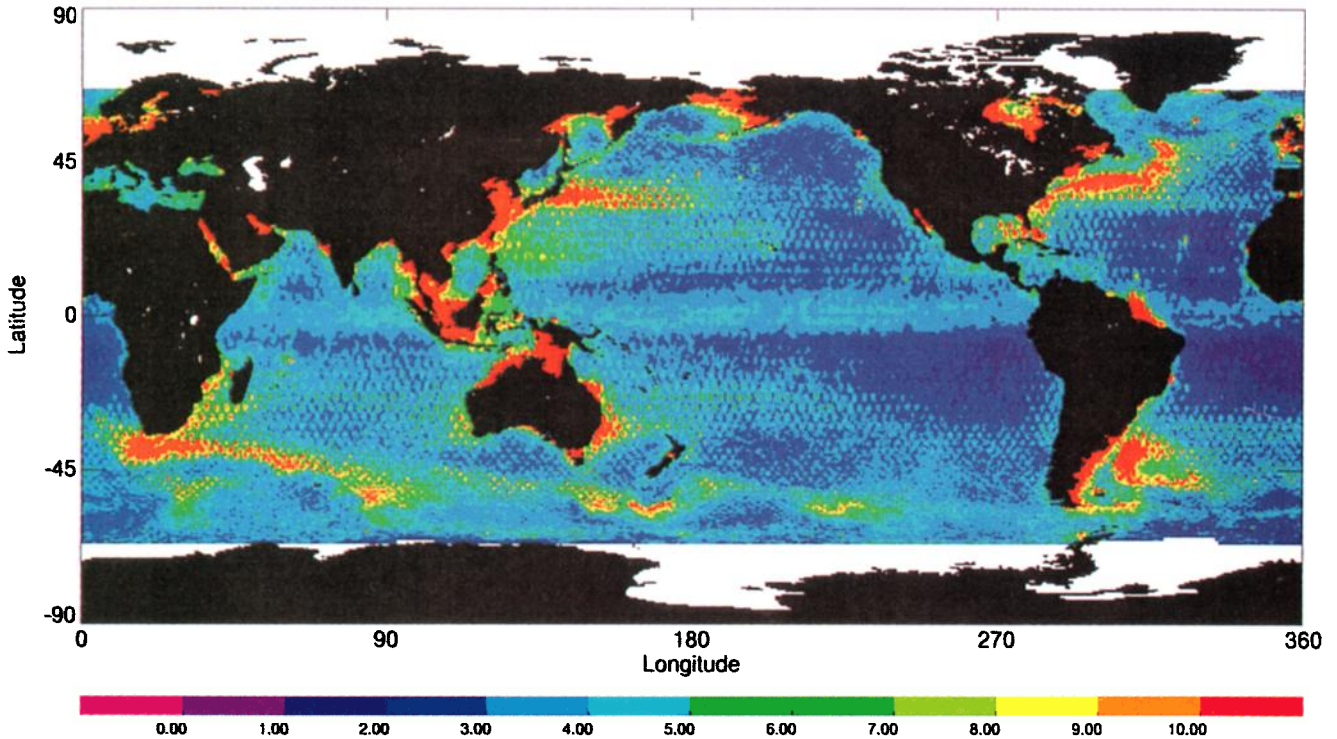


**Plate 1.** Rms of the SLA differences between T/P and ERS-1 and -2 gridded data. The data are suboptimally mapped through an objective analysis scheme on a regular 0.25° × 0.25° resolution grid. Maps from October 1992 to December 1993 and from March 1995 to October 1997 are used. Units are centimeters.

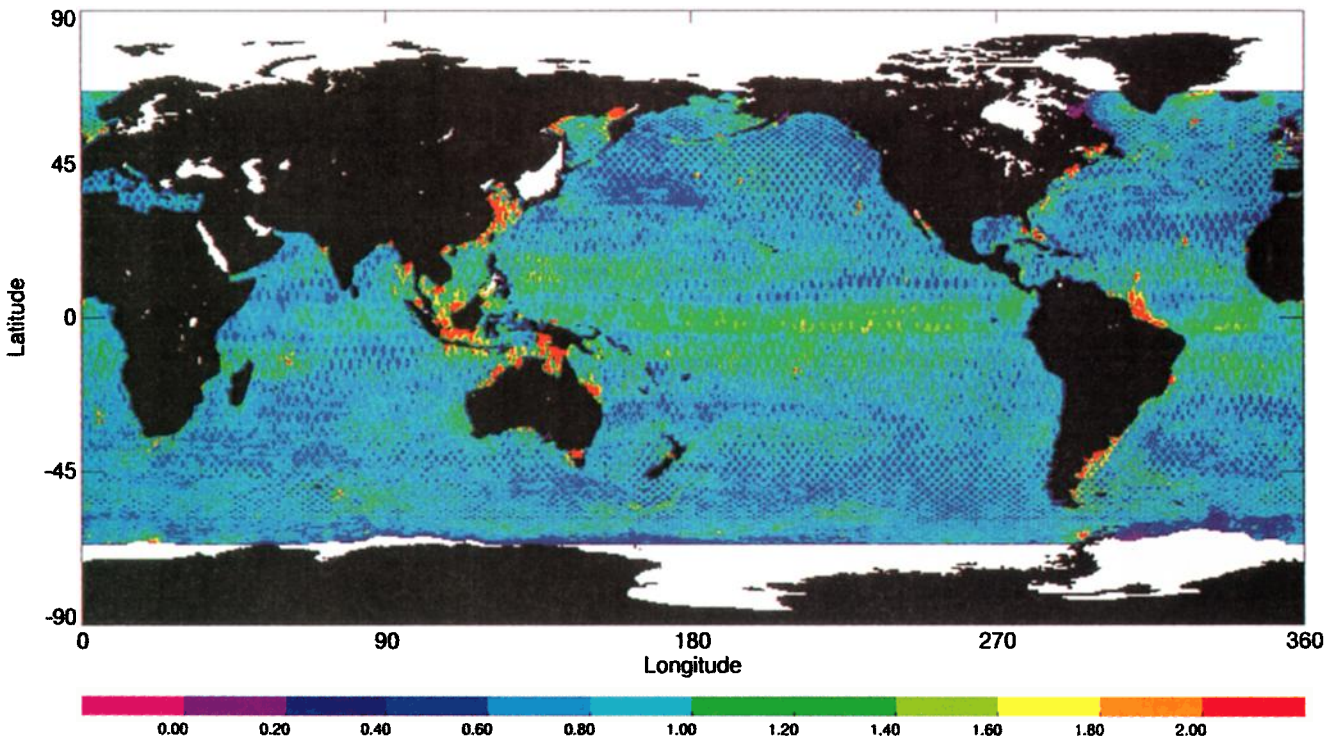


**Plate 2.** Same as Plate 1 but normalized by the sum of the mapping errors from the objective analysis (see text).

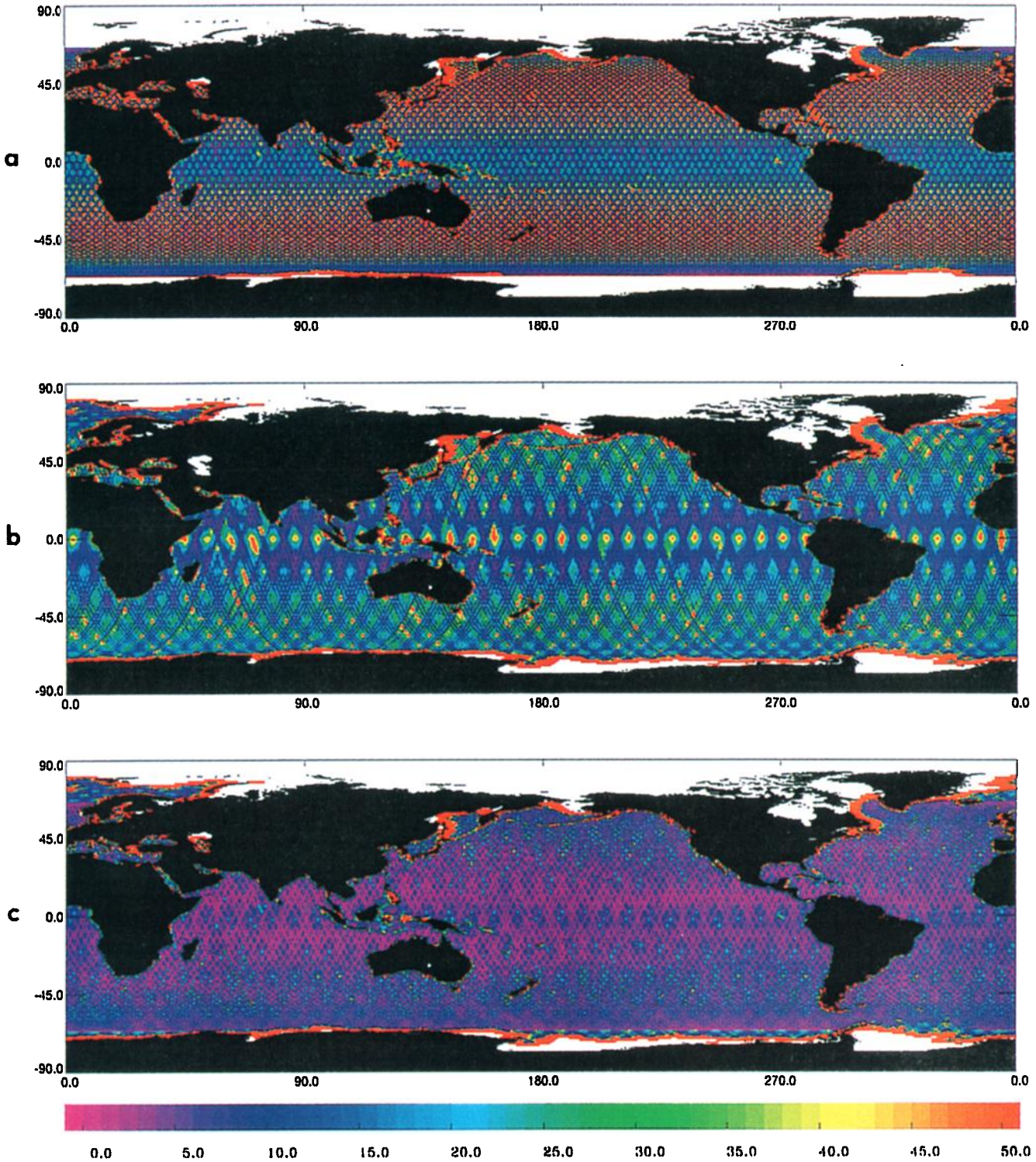


**Plate 3.** Mapping errors, in percent of the signal variance, as given by the objective analysis, for (a) T/P, (b) ERS-2, and (c) the combination of T/P and ERS-2, at an arbitrarily chosen date (February 8, 1997).

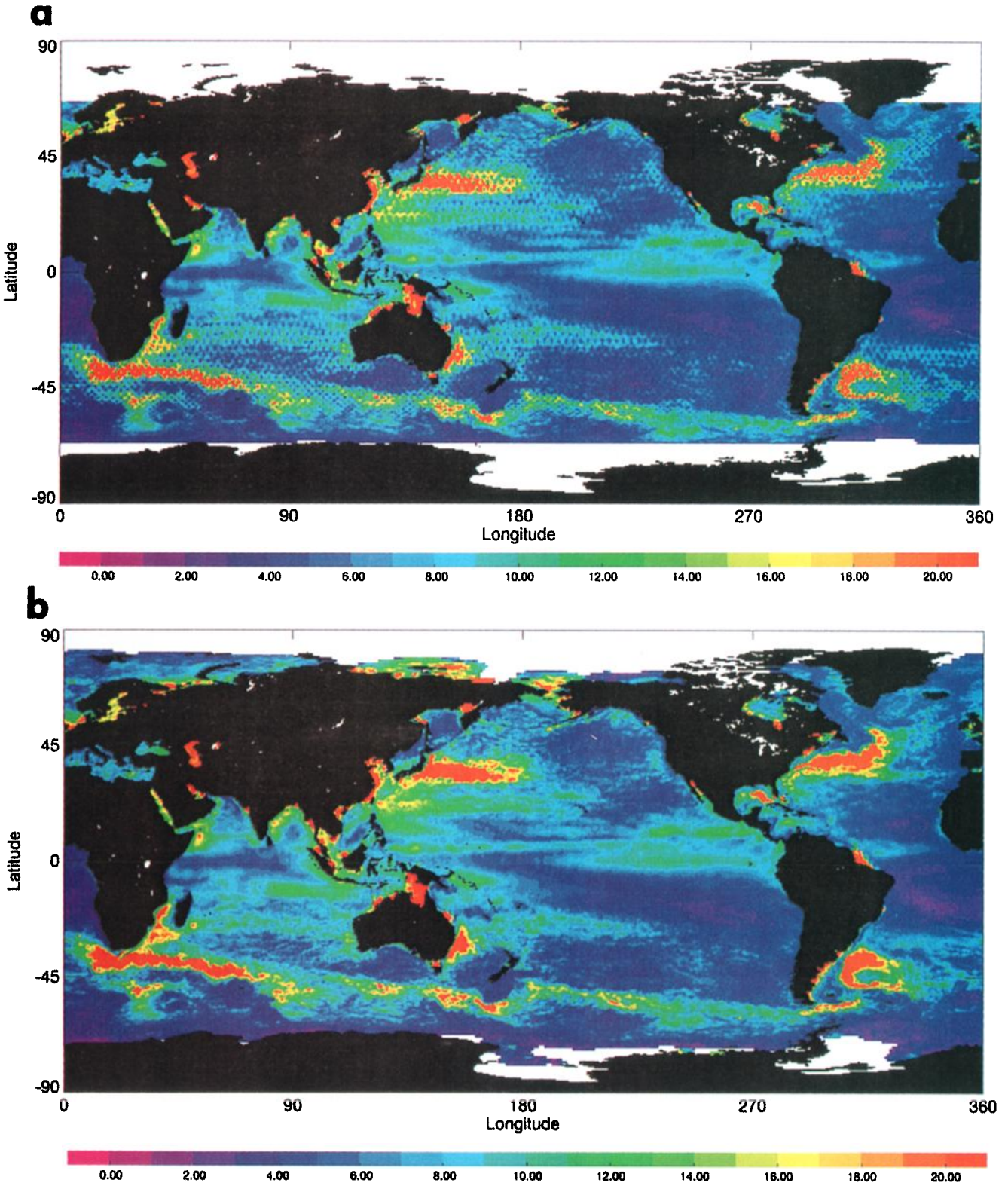


**Plate 4.** (a) T/P and (b) T/P + ERS-1/2 rms SLA variability over the same period as in Plate 1. Units are centimeters.

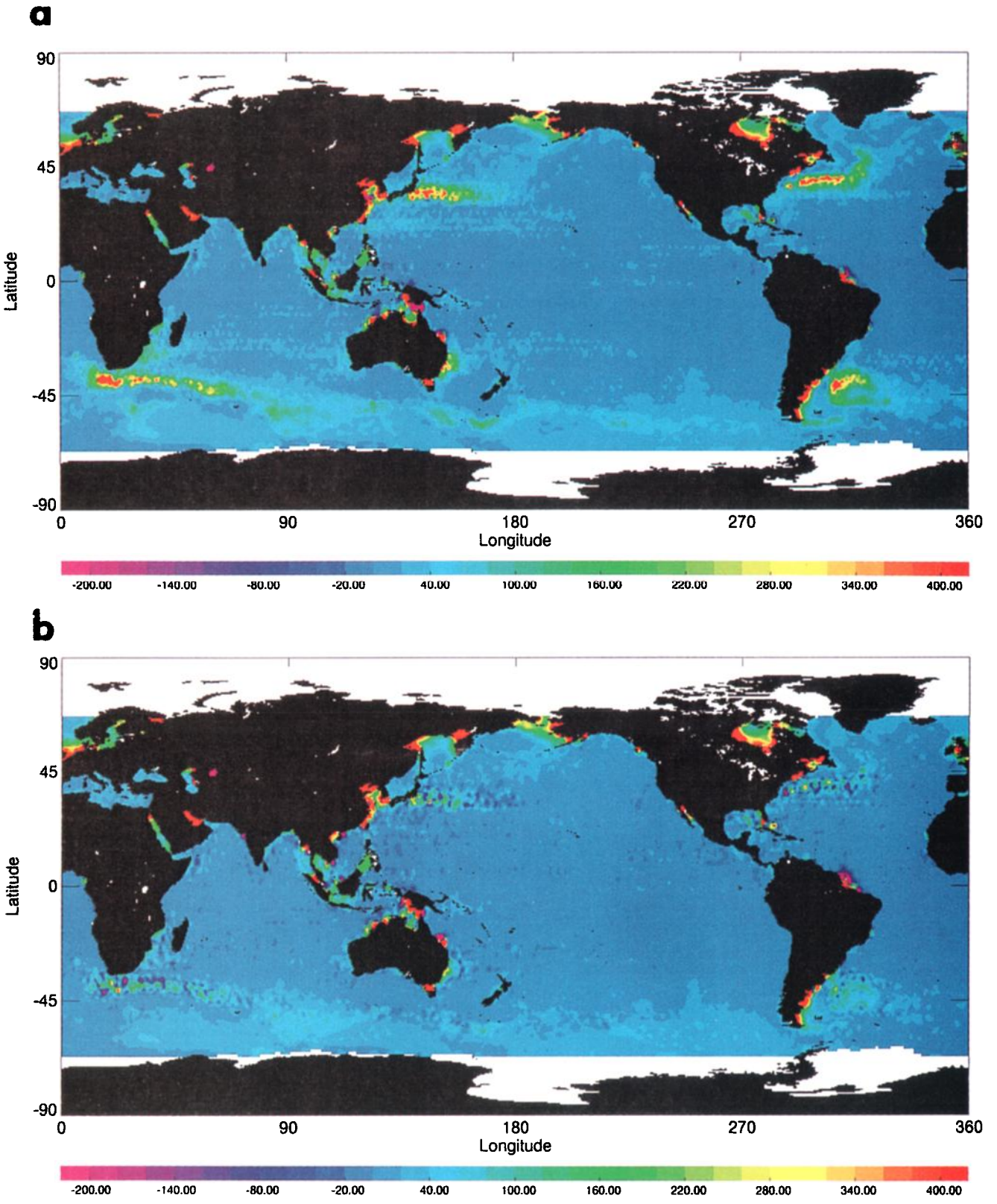


**Plate 5.** (a) Difference between T/P along-track SLA variance and T/P mapped SLA variance. (b) Same as Plate 5a but between T/P along-track data and combined maps. On the basis of T/P altimetric along-track data during the same period as for Plate 1 (cycles 4–45 and 94–188). The along-track variance map corresponds to values first evaluated along the T/P ground tracks. Then both along-track variance and mapped SLA variance are subsequently gridded using a weighted interpolation with a decorrelation scale of 2° in latitude and longitude. Units are $cm^2$.

the SLA in equatorial and tropical regions, and the reduction in scale of mesoscale eddies with latitude (variation in internal Rossby radius, as discussed by *Stammer* [1997]). The temporal correlation scale is set to 15 days at midlatitudes and decreases linearly from 15 to 10 days between 10°N/°S and 5°N/°S. Smaller time correlation scales at the equator (10 days between 5°N and 5°S) are suitable because of faster ocean dynamics.

The data error is the sum of a white noise uncorrelated between different data and a long wavelength error correlated along a particular track for a given cycle. The white noise is computed assuming a measurement noise of 2 cm rms for T/P and 3 cm rms for ERS taking into account the reduction due to smoothing. The long-wavelength error is taken as a uniform error of 3 cm rms for T/P and 4 cm rms for ERS (note that ERS data are adjusted onto T/P, which considerably reduces its long-wavelength errors). The variances of the white measurement noise and the long-wavelength error relative to the ocean signal variance are then calculated using an a priori estimate of the SLA variance calculated from ERS adjusted along-track data. The relative variance of long-wavelength error (i.e., $E_{LW}$, see appendix) varies between 1 and 2% in high-energy areas such as the Gulf Stream and can reach 40% in tropical areas and other low-energy areas. Further discussion on this method and on the sensitivity to the a priori choice of the long-wavelength error variance is provided by *Le Traon et al.* [1998].

We then computed SLA maps from October 1992 to May 1998. Because of the ERS geodetic mission, combined maps are missing from mid-December 1993 to the end of March 1995. There is one map every 10 days, and the grid resolution is 0.25° in latitude and longitude. The statistical comparisons performed in sections 3 and 4 are based on the first 5 years of data with the time period corresponding to the ERS-1 geodetic mission removed from the T/P data set. This eliminates the problem of T/P interannual variability from the 15 month gap biasing the statistical results.

## 3. Comparison of T/P and ERS-1 and -2

The rms variability of the differences between T/P and ERS-1/2 SLA maps is less than 2 or 3 cm rms in low-energy areas (Plate 1). This indicates a good consistency between the two data sets. This is due to the global adjustment of the ERS orbit onto the more precise T/P orbit and also to the improvement of the conventional objective analysis method, which results in correcting residual long-wavelength errors. In the major current systems the differences are larger but are mostly due to the differences in the sampling by the two satellites, ERS being able to observe eddies in-between T/P tracks. In these high–eddy energy areas, differences can be larger than 10 cm rms, and merging is then required to map the mesoscale oceanic signal.

If we normalize the variance of the SLA differences (T/P − ERS) by the sum of the error variances, we theoretically should obtain a number around one, assuming that T/P and ERS errors are not correlated with each other. Shown in Plate 2 is the mean relative error given by $[\langle(\mathrm{SLA}_{T/P} - \mathrm{SLA}_{ERS})^2\rangle / (\langle\varepsilon^2_{T/P}\rangle + \langle\varepsilon^2_{ERS}\rangle)]^{1/2}$, where the angle brackets stand for the time average, $\varepsilon_{T/P}$ and $\varepsilon_{ERS}$ are the error estimates as given by the objective analysis (see (2) in the appendix), and $\mathrm{SLA}_{T/P}$ and $\mathrm{SLA}_{ERS}$ are the measured SLAs by the respective satellite altimeters.

Globally, we obtain a ratio close to one. The small discrepancies can be due to an underestimate (overestimate) of the mapping errors that results if the chosen space and/or time correlation scales are too large (too small). For example, at the equator the time correlation of 10 days may still be too large compared to the timescales of the ocean dynamics. Alternatively, the correlation between T/P and ERS errors cannot be neglected in some areas: if, for example, there are too few valid satellite measurements to derive a realistic estimate of sea level, both errors will be strong and a fortiori correlated because they will include the same real ocean signal. This result is nevertheless very satisfactory. It means that most of the differences between the T/P and ERS-1 and -2 maps can be explained by sampling errors. It also means that mapping errors derived from the objective analysis are realistic and thus that the correlation scales were well chosen.

## 4. Contribution of the Merging

### 4.1. Mapping Error

Combining T/P and ERS data considerably reduces the a posteriori mapping error and homogenizes it. Plate 3 shows the errors given by the objective analysis (equation (2) in the appendix) as a percentage of signal variance for T/P, ERS-2, and the combination of both at the arbitrarily chosen February 8, 1997. Note that the error structures in these three cases are very different because of orbit configuration differences. Because the T/P repeat period is short compared to the a priori timescale of 15 days (except in an equatorial band of 5°N/°S where it is reduced to 10 days), T/P error is very homogeneous in time but has large spatial variability. The map of Plate 3a presents the classical "diamond structure" of the error estimation field, with the maximum occurring at the center of the diamond. Its value ranges from about 20% of the signal variance at the equator and increases with latitude to reach ~80% around 40°N/°S because of smaller spatial correlation scales. Indeed, at 40°N/°S the T/P intertrack distance is ~240 km compared to a spatial correlation of ~140 km representing the typical size of mesoscale eddies at those latitudes. At very high latitudes (higher than 50°N/°S), as T/P ground tracks get closer to one another, the mapping error decreases to typical values of ~30% at 60°N/°S. The ERS error pattern is more complex, showing both space and time variability (Plate 3b). Along the equator the regularly spaced red spots associated with errors greater than 50% are mainly due to ERS time sampling and the fact that two geographically adjacent tracks are separated by a time lag of up to 16 days. Here the choice of a 10 day time correlation is too short compared to the ERS temporal resolution. Plate 3c shows that the error associated with the combination of both satellites is significantly more homogeneous and reduced. We now get SLA field mean mapping errors below 10% of the signal variance, which means that the information provided by the two satellites is clearly complementary. Compared to T/P only, the combination of T/P and ERS reduces the mean mapping error by a factor of more than 2 (from 25% of the signal variance for T/P to less than 10% for the combined maps). This large improvement is described in more detail by LD99, who also provide a thorough discussion on the apparently contradictory conclusions of *Greenslade et al.* [1997] on the mesoscale mapping capability of multiple altimeter data sets. The mapping errors show that the combination of T/P and ERS provides a good mapping of the mesoscale variability; errors are small compared to the ocean signal and should have

only a minor impact on the oceanographic interpretation of T/P + ERS SLA maps.

### 4.2. Sea Level Variability

One way to assess the contribution of the merging of the two data sets to the mapping of mesoscale ocean signals is to compare the rms SLA variability obtained from T/P data only and from the combined data. One notices unrealistic features on the T/P map, mainly in high ocean variability regions, where the rms erroneously changes from one grid point to the next (Plate 4a). This is somewhat expected as we have chosen spatial correlation scales that are assumed to represent the mesoscale ocean signal and the T/P orbit was optimized for large-scale ocean signal observation. Its large intertrack distance of 2.8° does not allow an adequate mapping of the mesoscale ocean circulation variability. This problem disappears when combining T/P with ERS data since the merging should help resolve the mesoscale (Plate 4b). One can already note the high level of detail that is revealed by this map over the global ocean, which will be discussed in section 6.1 from the EKE point of view.

A second validation test is to compare the SLA variability derived from the maps and from the along-track data. We use T/P along-track SLA data, which span the period from cycles 4–45 and 94–188, to correspond exactly with the available dates of the combined maps. The along-track data are filtered as described in section 2.1 to be comparable with the maps. Almost all the studies on ocean eddies based on altimetric data use along-track SLA rms maps [see, e.g., *Stammer*, 1997; *Qiu*, 1999]. So, understanding how the merging contributes to the reduction of discrepancies between along-track and interpolated maps is interesting. For this we use two different techniques. On the one hand, the temporal variance is computed at each grid point of the combined maps (which are obtained by applying the optimal interpolation scheme to the along-track data). On the other hand, the map of the along-track variance results from first computing the signal time variance at each point along the satellite track, which is the more accurate way to do it, and subsequently mapping it on the same $\frac{1°}{4}$ regular grid. Because of the large intertrack distances with T/P, a weighted interpolation is then applied to map the ocean signal: each 1° × 1° grid point estimate is the weighted average of the points contained in a 2° × 2° box, the weight being proportional to their distance to the grid point. We expect the variance deduced from the T/P maps to be weaker than those from along-track data, which is clearly displayed in Plate 5a. In high-variability regions where differences can reach up to 600 $cm^2$ (~25% of the oceanic variance in these areas), T/P-interpolated maps considerably underestimate the variability. The difference between the T/P along-track SLA variance and the combined mapped variance shows that almost all the previous discrepancies disappear, displaying very small and homogeneous differences (Plate 5b). This is also a first indication of the good precision of the mapping. We thus expect that most ocean eddy energy will be conserved in the combined maps.

At high latitudes, where the ocean is not highly variable at the scales resolved, the differences between along-track data and maps can nevertheless be significant. In the Southern Ocean, between 50° and 60°S, south of the Antarctic Circumpolar Current, they can reach up to 40 $cm^2$. This difference is probably due to residual inverse barometer errors or high-frequency barotropic variability, which is expected to be large at high latitudes [*Stammer et al.*, 2000; *Tierney et al.*, 2000], and demonstrates the effectiveness of the long-wavelength error correction. The same can be noticed in the Bering Sea, at 55°–60°N and 170°W, where the strong differences of up to 250 $cm^2$ correspond to well-known residual tidal errors present in the along-track data, which were partly corrected by the optimal interpolation.

### 4.3. Geostrophic Velocity

**4.3.1. Velocity mapping error.** Surface geostrophic velocities are usually obtained from along-track SLA, and only their cross-track component can then be obtained. With the mapped data we have the opportunity to get information on zonal and meridional geostrophic velocities independently and study ocean anisotropy. Mapping the velocity field is, however, very demanding in terms of sampling. Quantifying the mapping errors on the zonal ($U'_g$) and meridional ($V'_g$) geostrophic velocities before interpreting the results is therefore necessary. This can be done with the same mapping procedure by modifying the correlation function between the field to be mapped and the observations. Such an analysis is performed by LD99. They show that the T/P + ERS quadratic mapping error on velocity is about 20% of the signal variance and that the error is more homogenous than for the SLA. The mapping errors on the velocity field are thus twice as large as for the SLA; they remain, however, small (although not negligible) compared to the signal variance. This means that they will not impact much our interpretation of $\langle U'^2_g \rangle$, $\langle V'^2_g \rangle$, or EKE maps. LD99 also show that the mapping error on the meridional velocity ($V'_g$) is only slightly larger (by a few percent) than the error on the zonal velocity ($U'_g$). The impact on isotropy analyses should thus also be small. From (1) in the appendix, showing that the a posteriori variance of the mapped field is equal to the true (unknown) variance minus the mapping error variance is easy. This means that the velocity variances and EKE derived from the combined maps are likely to be underestimated by ~20%. The velocity maps derived from T/P only have a mean mapping error of ~40 ($U'_g$) and 50% ($V'_g$) (LD99). Compared to the combined maps, they should underestimate the velocity variances by about 30–50%, which will be confirmed below.

**4.3.2. Contribution of the merging.** To evaluate the contribution of the merged data set to the velocity calculations, we compute the zonal and meridional velocities derived from the T/P only and T/P + ERS combined maps every 10 days and compare their variance over the period of the combined data. The grid on which we estimate the interpolated SLA from the objective analysis has a resolution of −1/4° by 1/4°, which does not represent a constant spatial grid spacing in longitude: 0.5° represents ~55 km at the equator, 28 km at 60°N/°S, and ~5 km at 80°N/°S. To study further the isotropy of the velocity field, that the SLA gradients in the zonal and meridional directions be calculated over the same distance is necessary. Therefore we resampled the maps using a cubic spline interpolation based on the five closest points surrounding the estimated grid point. Velocities were subsequently calculated from the slope of the SLA data determined by a centered difference scheme over a 30 km distance. In strong variability areas, zonal velocity variances are then ~10% higher than when based on SLA slopes over 0.5° in latitude. Because of small values of the Coriolis parameter near the equator, geostrophic velocities were not calculated in the ±5° equatorial band. The calculation of the velocity field in the equatorial band, following *Picaut et al.* [1990], requires a specific space and time filtering that is beyond the scope of this paper.

The variances of either the zonal ($\langle U_g'^2 \rangle$) or the meridional ($\langle V_g'^2 \rangle$) geostrophic velocity, inferred from the combined data, represent well the five major current systems (not shown), the maximum mean variance being found in the western boundary currents, reaching up to 4500 $cm^2\ s^{-2}$ either for $\langle U_g'^2 \rangle$ or $\langle V_g'^2 \rangle$. We then compare those maps with those of T/P only. The maximum differences, found in the Gulf Stream and the Kuroshio, are more than 1500 $cm^2\ s^{-2}$ (Plates 6a and 6b), meaning that the merged data observe 30% more of the velocity variance than T/P only. On Plate 6a, T/P tracks are present, as expected, because of the fact that sea level gradients are not well estimated with T/P only (see discussion in 4.2). On the $\langle V_g'^2 \rangle$ map (Plate 6b) the vertical structures are explained by the fact that zonal gradients are better estimated close to cross-over points; in other words, if the T/P orbit inclination were 45°, instead of ~66°, there would not be any asymmetry between the zonal and meridional velocities. The merged product also helps reduce this phenomenon, so that the asymmetry almost disappears on the combined maps (not shown).

### 4.4. SLA Spectra

To analyze further the merging contribution, mean wavenumber spectra derived from the gridded SLA data (T/P and T/P + ERS-1) were computed in different regions of the world ocean, such as low-variability areas (northeastern Atlantic), the Antarctic Circumpolar Current, and the western boundary currents. The qualitative conclusions for all these areas being similar, we present here the mean spectrum in the Gulf Stream region (33°–43°N, 70°–50°W) for the year 1993. Spectra were computed in both the zonal and meridional directions. According to the decorrelation scales in space and time in this region (see section 2.2) the number of degrees of freedom is greater than 120, which corresponds to a precision of ~20% in the spectra. Figure 1 shows the two (T/P and T/P + ERS-1) spectra for the zonal direction as well as the T/P + ERS-1 mean spectrum in the meridional direction. A mean T/P along-track SLA spectrum is also shown as a reference.

The comparison between T/P and T/P + ERS zonal spectra shows that the latter contains more energy than the former at all wavelengths. This was somewhat unexpected for the long wavelengths (above 500 km), which should also be well observed by T/P alone. However, this result is very sensitive to the choice of the correlation scale used for the mapping because of the inadequate T/P sampling in the zonal direction (see the large mapping error in Plate 3a). A separate study was undertaken, slightly increasing the objective analysis correlation scales (from 150 km to ~200 km). This reduces the energy in the mesoscale band, as expected, but also gives more energy at longer wavelengths (between 400 and 800 km). In this case the T/P mean spectrum contains the same energy as for the combined maps at wavelengths larger than 500 km.

The comparison with the spectrum of T/P along-track data shows that the combined maps have an energy similar to the along-track data at wavelengths larger than ~150 km. For wavelengths larger than ~400 km the combined map spectrum is less energetic than the along-track one. This does not mean that the combined maps are missing some energy at these wavelengths but rather suggests that the distribution of energy in the Gulf Stream is not fully isotropic; there is more energy in the meridional direction (closer to the T/P tracks inclination) than in the zonal direction. This is confirmed by the analysis of the mean spectrum derived from the combined maps in the meridional direction (Figure 1). For wavelengths of less than 150 km the spectrum of combined data has less energy than the along-track T/P spectrum, even though the integrated energy contained between both curves is low (~2 cm rms between 100 and 200 km). This not only results from the mapping procedure but also from the filtering of along-track data before the mapping (which uses a cutoff of 100 km at these latitudes, affecting wavelengths up to 200 km).

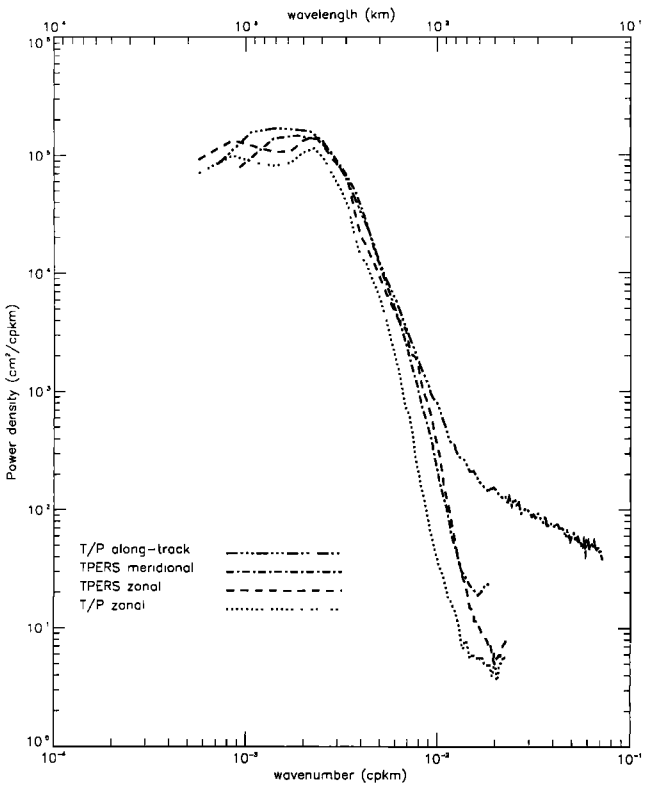


**Figure 1.** The 1993 mean wavenumber spectra in the Gulf Stream region (33°–43°N; 70°–50°W) of the along-track SLA data (dash-dot-dot-dot) compared with the zonal component of the T/P maps (dotted) and the zonal (dashed) and meridional (dash-dot) components of the combined maps.

Thus the combination of T/P and ERS recovers signals with wavelengths larger than 150–200 km, in particular zonally. This is obviously not achieved with T/P data alone and is an important contribution of the merging of T/P and ERS data.

## 5. Validation With in Situ Measurements

As it will be the basis of most of the following descriptive analyses, a careful validation of the geostrophic velocity calculation is needed to ensure that the energy level contained in the maps is correct. Indeed, the energy level is strongly related to the spatial filtering and could be also affected by the mapping procedure itself (see section 4). Several previous studies showed comparisons between altimetry and in situ measurements [*Zlotnicki et al.*, 1993; *Picaut et al.*, 1990; *Strub et al.*, 1997; *Wunsch*, 1997; *Kelly et al.*, 1998; *Stammer and Wunsch*, 1999]. When all these studies are viewed together, it is clear that the altimetrically derived geostrophic velocities seldom have correlations below 0.5 or higher than 0.9 when compared with shallow current meters or Doppler profilers. In this section we compare the variability statistics of the combined prod-

uct with two sets of data: on the one hand, mapped statistics of estimated surface geostrophic EKE from World Ocean Circulation Experiment (WOCE) drifters in the North Atlantic, and on the other hand, rms variability from shallow current meters on a few moorings. The moorings produce a pointwise comparison for a limited stretch of time that samples a few particular oceanic regimes and may thus not be representative of a larger area (e.g., local effects due to bathymetry). There is also an issue of estimating the velocity at the surface [*Wunsch*, 1997], which is not relevant in our study given the shallow depths of the selected moorings. The drifters provide a mapping and therefore can be used for a comparison of the spatial distribution of variability. On the other hand, the drifter data used to create the maps are not all simultaneous to the T/P + ERS combined product and have irregular time and space sampling. Furthermore, there is an issue of estimating and removing the nongeostrophic component of variability.

### 5.1. Surface Drifters

The data set used here contains data of 1159 WOCE drifters drogued at 15 m from 1991 to January 1999 in the Atlantic Ocean. The data have been processed at the Atlantic Oceanographic and Meteorological Laboratory (AOML), and time series resulting from a krigging analysis are provided at 6 hourly intervals [*Hansen and Poulain*, 1996]. The drift characteristics of the surface velocity profilers (SVP) drifters have been carefully investigated [*Niiler et al.*, 1987, 1995] and determined to have a downwind slip close to 0.05 (0.07) cm $s^{-1}$ (m $s^{-1})^{-1}$ of wind speed relative to the current at 15 m [*Niiler et al.*, 1987, 1995]. Detection of drogue loss is automatically done at AOML, and these data are removed (we detected an additional two drifters having lost their drogue, when investigating drifter data in 1993 in the Azores Current during Structure des Echanges Mer-Atmosphere, Proprietes des Heterogeneites Oceaniques: Recherche Experimentale (SEMAPHORE) [*Eymard et al.*, 1996]). This suggests that there are still a few errors in the data set but at a level unlikely to influence the results significantly. In addition, we included 60 drifters drogued at 50 m depth and deployed in the Labrador Sea for the Ice Patrol (these drifters are assumed to have retained their drogue, which could not be checked). Filtering of inertial motion and other high-frequency nongeostrophic motions was done by applying a Lanczos filter with cutoff at 2 days. The variance associated with the Ekman component of the drifts was estimated from ECMWF daily winds (see below).

The number of data included in this set is much higher than in earlier analyses based on the order of a hundred floats [*Richardson*, 1983; *Brügge*, 1995]. The data were gridded on a 0.5° × 1° grid to retain the fine resolution that the number of observations permits in a large part of the North Atlantic. The data distribution is not homogeneous (more drifters having been deployed north of the Gulf Stream, close to Iceland, and in the Azores Current). Drifters will also tend to sample preferentially convergent features and therefore also fronts. These effects will result in biases in the mean field. In that sense it is reassuring to find similar features in the average circulation to the ones presented by *Brügge* [1995] using a different set of drifters, all drogued at 100 m. The effect should be much less severe for the variability, and here we will assume that the data set provides a quasi-Eulerian sampling of the eddy field (precisely determining biases in the variance fields is a complicated issue that requires important modeling effort). Uncertainty due to the sampling of the variance field is large, often a factor 2, as was found when comparing estimates based on half the floats or separated seasons. The large-scale features of the field are nonetheless robust except in the southern and southwestern parts of the subtropical gyre, the Gulf of Mexico, and the Gulf Stream south of 36°N and shortly downstream of Cape Hatteras (the drifters enter the stream mostly from the slope current to the north).

Differences between the variance estimates in this set and the one in the geostrophic current arise because of the ageostrophic component in the buoy drift. *Van Meurs and Niiler* [1997] have illustrated how the stationary wind-driven component of the buoy drift could be estimated from the wind stress. We have applied this formula with an additional scaling in latitude as the square root of the Coriolis parameter (P. Niiler and E. Ralph, personal communication, 1997) on daily fields of the 1989–1993 ECMWF reanalysis. The variance in this component of the current corresponds to the maximum EKE of 20 $cm^2$ $s^{-2}$, close to New England and south of Greenland between 10 and 20 $cm^2$ $s^{-2}$ at midlatitudes and south of 10°N, and less in the subtropics. This is rather uncertain but is small compared to the surface EKE in most of the Atlantic and therefore has a small effect on the comparison with the T/P + ERS combined maps. The values found in this drifter set are comparable to the values by *Brügge* [1995] for the North Atlantic Current branches and in the subpolar gyre. The maximum values we have in the Gulf Stream are larger by up to a factor 2 compared to *Richardson* [1983]. This might be caused by the coarse resolution of this earlier product.

The rms variabilities presented in Plate 7 (left) for the northwest Atlantic are rather noisy because of the often small number of drifter data in each box (even with 25 days of data, which is reached by only ~40% of the boxes, the 90% uncertainty range on $\sigma$ is probably between 0.6 and 1.4). Nonetheless, the maps of rms variability present striking similarities with the ones in the combined product for both velocity components, even at a fairly high level of detail. The maxima of variance in the Gulf Stream are comparable, being only 20% larger in the drifter set. Visually, variance in the Gulf Stream seems larger for $U'_g$ in the drifter set (see in the North Atlantic Current, near 50°N, between 315° and 340°E) and for $V'_g$ in the T/P + ERS mapped product (e.g., in the Gulf Stream, at 39°N). There is also a tendency for the variance to be larger in the drifter set in the subpolar gyre (see, e.g., the patch of large values in the drifter product near 61°–62°N off west Greenland). We also present the comparison as a scatter diagram both for the zonal and meridional components (Figure 2). Figures 2a and 2b present a clear correlation between the two sets with an alignment of the data along the axis of equal values (we have retained only values with more than 25 days of drifter observations). The tendency, however, for more $V'_g$ variance and less $U'_g$ variance in the T/P + ERS product for large velocity rms variability is confirmed. As was mentioned in section 4.3.1, we do not expect a large bias in the ratio between $U'_g$ and $V'_g$ variance in this product, although it is possible that there is a residual of the effect related to the inclination of the orbit. LD99 show that the mapping of the meridional component of the geostrophic velocity is less accurate than the mapping of its zonal component but by only 10–20%. This is too small to account for the discrepancies in $U'_g$ and $V'_g$. We do not see clear reasons for this difference, which reaches more than 20% in rms($U'_g$) or rms($V'_g$), even though part of these discrepancies might result from the insufficient sampling in the drifter set and the nonsimultaneity of both data sets.

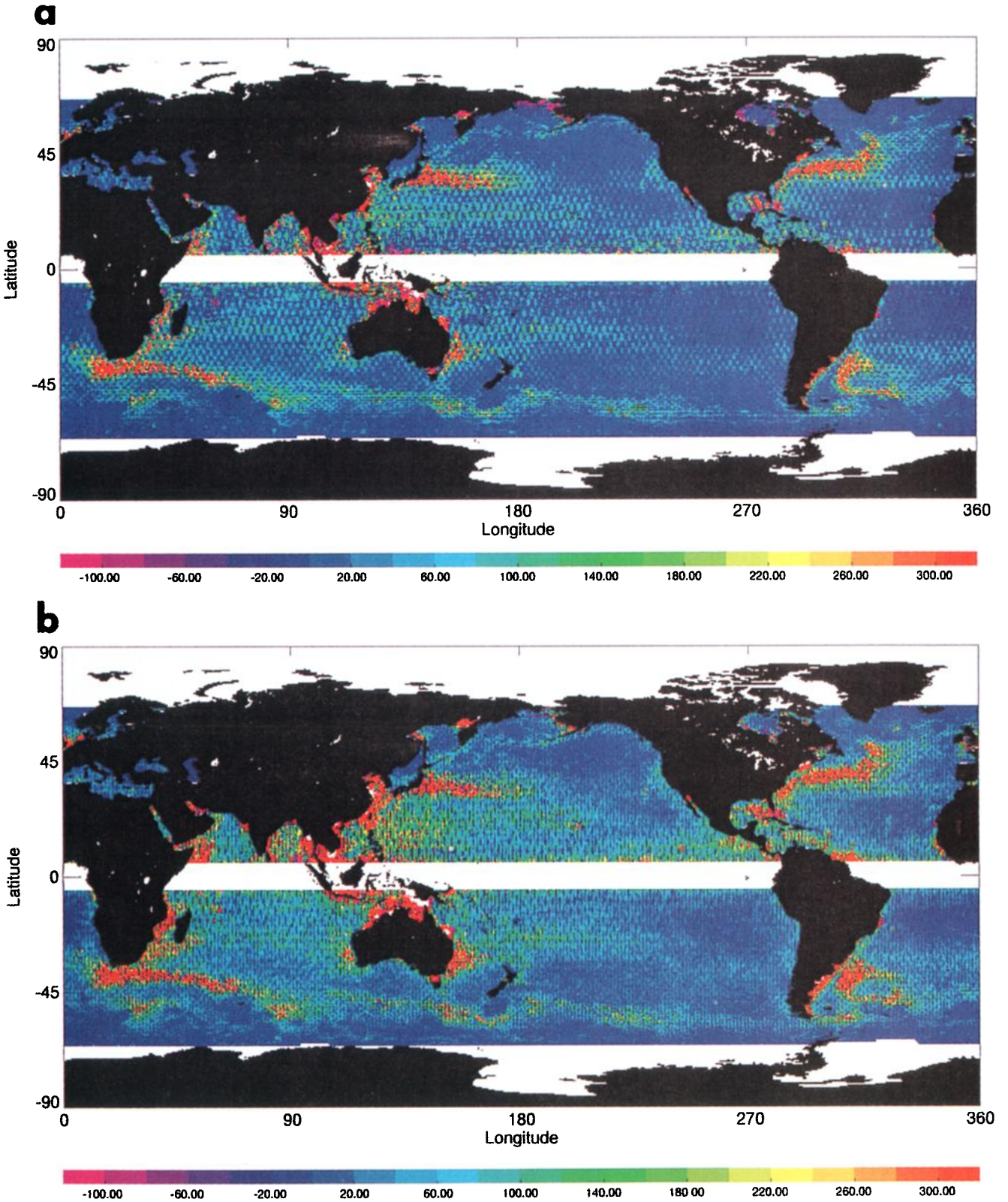


**Plate 6.** Differences between the combined maps and T/P maps for the (a) zonal and (b) meridional velocity variances. Units are $cm^2\ s^{-2}$. SLA gradients are calculated over a distance of 30 km (see text).

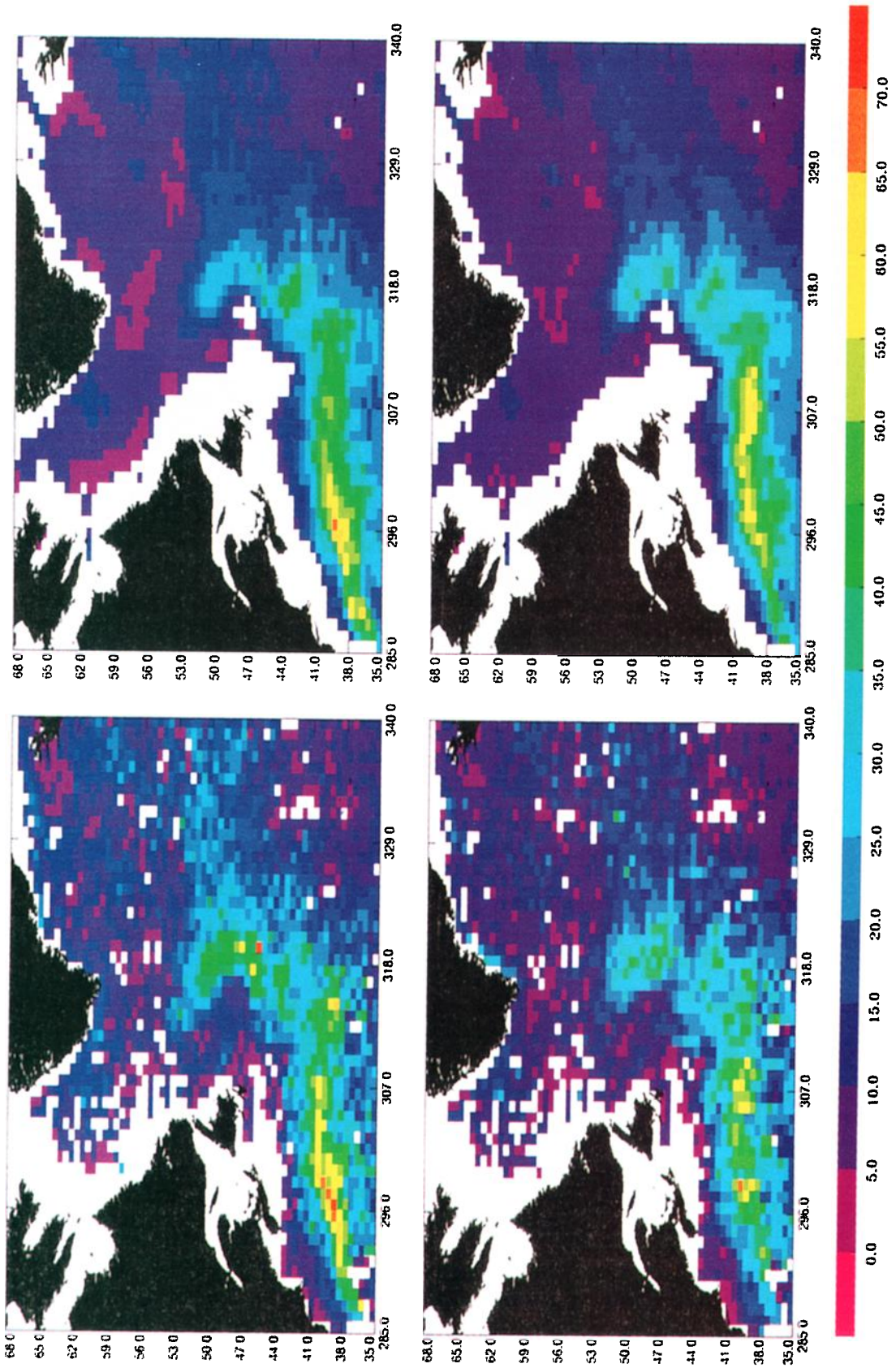


**Plate 7.** Rms of the zonal $U'_g$ (top) and the meridional $V'_g$ (bottom) components of the geostrophic surface velocity for the WOCE drifters (left) and the combined T/P + ERS-1/2 maps (right). Boxes with at least 25 days of data are kept for the drifters. Altimeter data over water depths >500 m are shown. Units are cm $s^{-1}$.

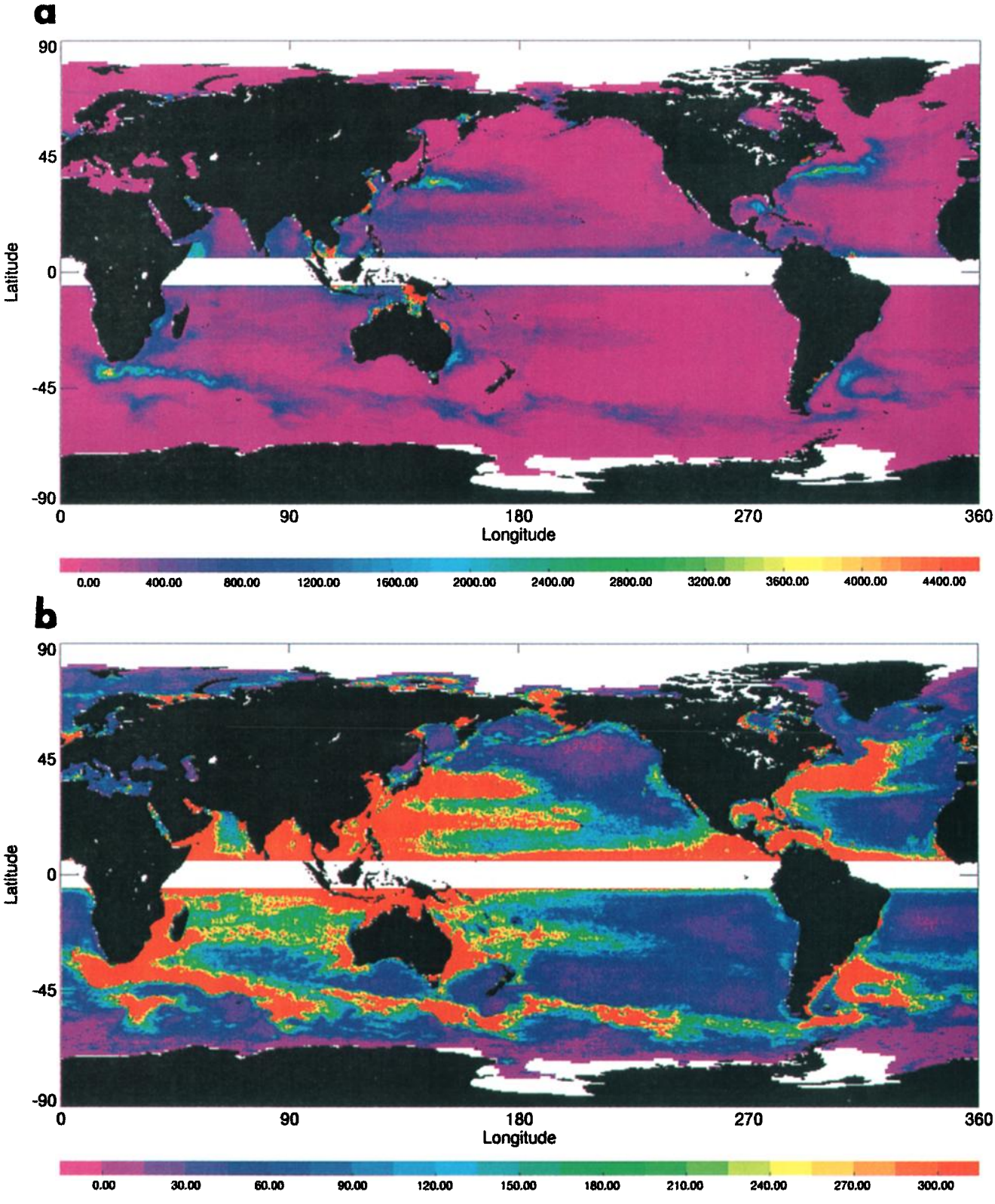


**Plate 8.** EKE, in $cm^2\ s^{-2}$, inferred from the 5 year period of both components of the geostrophic velocity variance. The color scale reaches (a) 4500 and (b) 300 $cm^2\ s^{-2}$.

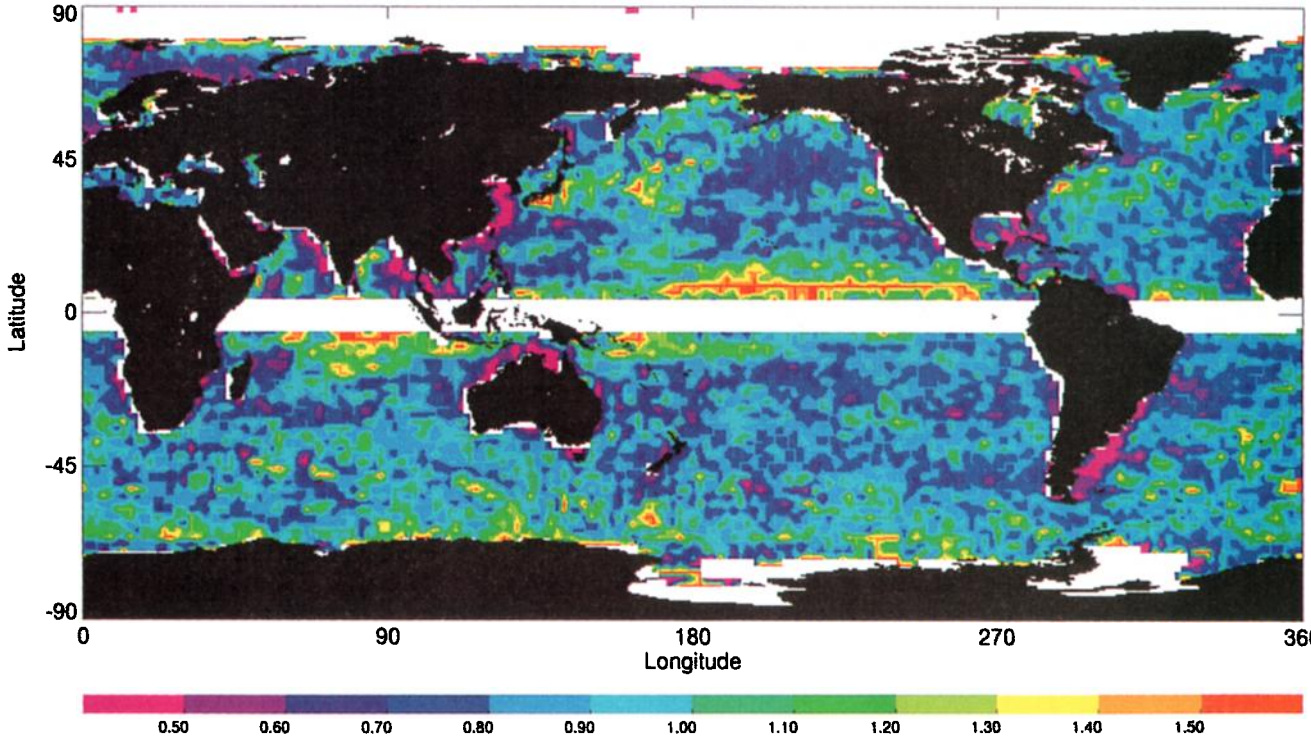


**Plate 9.** Ratio of $\langle U_g'^2 \rangle / \langle V_g'^2 \rangle$ over the same period as in Plate 1, after smoothing in 2° × 2° geographical boxes.

### 5.2. Current Meters

Few of the many publicly available current meter records match the conditions for a rigorous comparison with satellite observations. Ideally, mooring measurements should be close to the surface but below the Ekman layer (typically between 30 and 100 m in the subtropics, down to 200 m at higher latitudes). *Wunsch* [1997] presents a synthesis of surface EKE from earlier mooring data. Those data are not synchroneous with the T/P + ERS product. The comparison (not presented) presents a large scatter, part of it resulting from the nonsimultaneity between the two sets of data, and part of it probably resulting from uncertainty in the derivation of surface EKE from subsurface current meter records.

We therefore restricted the comparison to the few current meter records that were collected during the period of analysis of altimetric data and present comparisons done for the period of the record. Out of the moorings Table 1, some are from the northeastern subtropical North Atlantic (from experiments SEMAPHORE [*Tychensky et al.*, 1998] and Subduction [*Brink et al.*, 1995]); others are from the eastern boundary current regions, the tropical Indian Ocean, and other highly energetic areas. The comparison has been done mostly on the rms variability in $U_g'$ and $V_g'$ after filtering high frequencies but also on correlation when time series were available. We find a close agreement between the rms variability both for $U_g'$ and $V_g'$. In some cases, even the ratio rms($U_g'$)/rms($V_g'$) is fairly close,

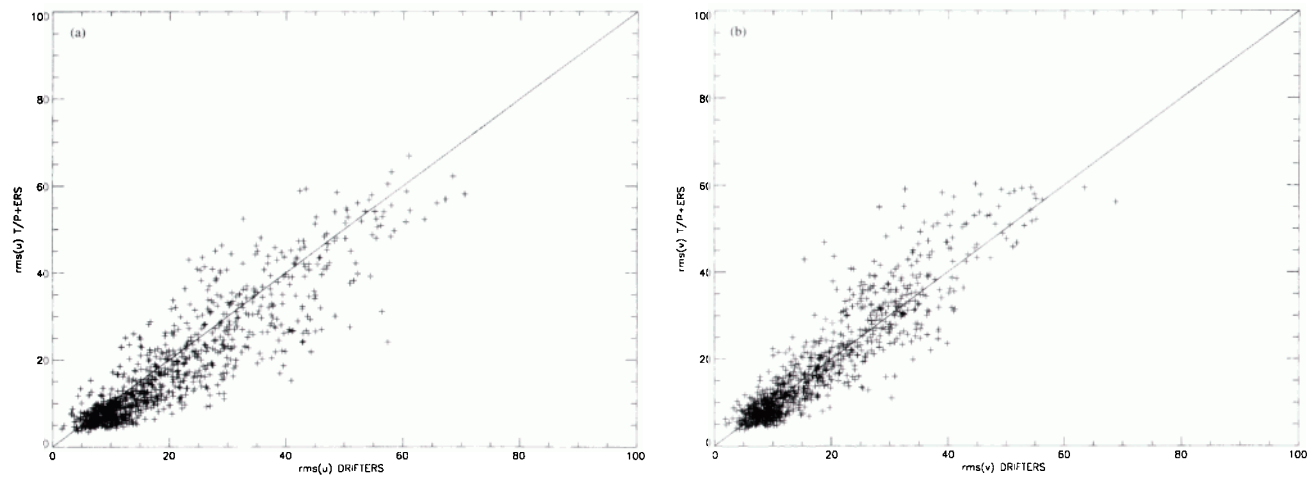


**Figure 2.** Scatter diagram of the rms of (a) $U_g'$ and (b) $V_g'$ between the WOCE drifters and T/P + ERS-1 and -2. Only boxes with more than 25 days of drifter data are kept.

**Table 1.** Comparison of Variability in Current Meter Data and in Simultaneous Currents From the T/P + ERS Analysis

| Site | Depth | Bottom | Period | Program | rms ($u$) Mooring | rms ($u$) T/P+ERS | Correlation | rms ($v$) Mooring | rms ($v$) T/P+ERS | Correlation | rms($u$)/rms($v$) Mooring | rms($u$)/rms($v$) T/P+ERS |
|---|---|---|---|---|---|---|---|---|---|---|---|---|
| 22.7°W/32.3°N | 170 | | July 1, 1993, to November 31, 1993 | SEMAPHORE | 5.0 | 5.3 | | 9.6 | 11.0 | | 0.52 | 0.48 |
| 23.4°W/33.7°N | 174 | | July 1, 1993, to November 31, 1993 | SEMAPHORE | 7.6 | 6.7 | | 14.4 | 14.4 | | 0.53 | 0.46 |
| 21.3°W/34.8°N | 143 | | July 1, 1993, to November 31, 1993 | SEMAPHORE | 4.9 | 4.9 | | 5.9 | 5.2 | | 0.83 | 0.94 |
| 29.0°W/25.5°N | 30 | 5670 | October 15, 1992, to June 16, 1993 | SUBDUCTION | 6.3 | 4.6 | 0.70 | 3.8 | 5.2 | 0.33 | 1.66 | 0.87 |
| 22.0°W/18.0°N | 30 | 3300 | October 7, 1992, to June 19, 1993 | SUBDUCTION | 3.7 | 4.3 | 0.36 | 3.9 | 4.8 | 0.42 | 0.95 | 0.89 |
| 33.9°W/18.1°N | 30 | 5300 | October 16, 1992, to May 21, 1993 | SUBDUCTION | 6.0 | 4.1 | | 6.3 | 6.1 | | 0.95 | 0.67 |
| 22.0°W/33.0°N | 70 | 5270 | October 2, 1992, to June 14, 1993 | SUBDUCTION | 11.0 | 13.7 | 0.93 | 8.6 | 9.3 | 0.87 | 1.28 | 1.48 |
| 10.2°W/42.3°N | 56 | 2700 | May 29, 1993, to December 6, 1993 | MORENA | 1.8 | 4.0 | 0.31 | 2.7 | 5.9 | 0.33 | 0.67 | 0.68 |
| 76.1°W/26.5°N | 100 | 4807 | October 26, 1995, to November 2, 1996 | ACM1 | 21.0 | 18.8 | 0.77 | 14.6 | 14.5 | 0.14 | 1.43 | 1.30 |
| 27.0°W/34.5°S | 30 | 4325 | December 15, 1992, to December 6, 1993 | ACM13 | 11.2 | 7.5 | 0.43 | 7.0 | 6.9 | 0.36 | 1.60 | 1.09 |
| 153.5°W/30°S | 50 | 95 | October 23, 1992, to September 14, 1993 | PCM3 | 21.6 | 14.2 | | 12.5 | 31.9 | | 1.73 | 0.44 |
| 124.1°W/38.8°N | 50 | 1972 | May 22, 1993, to December 6, 1993 | EBC | 9.7 | 5.9 | 0.12 | 12.1 | 8.3 | 0.74 | 0.80 | 0.71 |
| 51.9°E/11.9°N | 48 | 1020 | March 29, 1995, to October 23, 1996 | ICM7 | 24.9 | 22.3 | | 28.5 | 29.3 | | 0.87 | 0.76 |
| 53.4°E/10.6°N | 50 | 4060 | April 1, 1995, to October 22, 1996 | ICM7 | 76.1 | 54.2 | | 34.8 | 30.3 | | 2.18 | 1.79 |
| 53.9°E/9.7°N | 50 | 4609 | April 3, 1995, to October 21, 1996 | ICM7 | 42.8 | 46.9 | | 51.8 | 33.7 | | 0.83 | 1.39 |
| 54.3°E/8.8°N | 50 | 4940 | April 9, 1995, to October 21, 1996 | ICM7 | 51.2 | 47.8 | | 50.5 | 44.2 | | 1.01 | 1.08 |
| 53.9°E/7.8°N | 50 | 5120 | April 10, 1995, to October 21, 1996 | ICM7 | 47.8 | 44.0 | | 43.8 | 41.8 | | 1.09 | 1.05 |
| 53.4°E/7.0°N | 49 | 5120 | April 11, 1995, to October 20, 1996 | ICM7 | 40.7 | 42.5 | | 44.9 | 51.2 | | 0.91 | 0.83 |

The current meter time series have been smoothed at least with a 2 day low-pass filter. When the time series were available, 10 day averages have been estimated, and the values presented correspond to these time series. The correlation coefficient with the corresponding time series from the gridded product is then also indicated. For each mooring the bottom depth is reported. Notice that some moorings are in shallow water, close to shelves: we do not expect the mapped analysis to be very accurate in these areas.

which suggests that the analysis has not modified that ratio. The correlations with the 10 day averaged current meter records are often significant, in particular for sites away from shelves and with a rather large variability (notice in particular the results of the Subduction mooring in the Azores Current at 22°W, 33°N in Table 1). These agreements are remarkable considering that the altimetric product includes spatial averaging on scales of at least 50 km and that the current meters are below the surface with a possible geostrophic shear in some cases to the surface (for example, for the SEMAPHORE moorings this effect could reach a 2 cm $s^{-1}$ rms and is often correlated with the current [*Hernandez et al.*, 1995]). Also note that this comparison could be slightly improved by choosing regional rather global correlation scales that would better match the local dynamics of the studied area. Large difference are found for two moorings. One in the Labrador Sea, where the variance in the mooring currents is larger, and the other in the East Australian Current. The results for the Labrador Sea confirm what was found in the comparison to the drifter; that is, the variability is underestimated in the T/P + ERS analysis. The mooring in the East Australian Current is too close to the coast (between 30 and 50 km off shore, in the shelf break) to retrieve any reliable information from the interpolation method. In this case a finer data selection could be done by editing altimetric measurements "too" close to the coast that are likely to contaminate the estimate in our analysis.

## 6. Statistics of the Variability

We have just seen that the combination of T/P and ERS-1 and -2 provides an accurate description of the ocean circulation, retaining the accuracy of T/P data but with a finer spatial resolution. The variability present in the combined maps was found to have rms variability in good agreement with in situ measurements. We now have a powerful altimetric product to perform detailed global mesoscale ocean analyses, study the variance of the zonal and meridional velocities independently, and intercompare different oceanic areas. An oceanographic analysis of the combined data set is now carried out, focusing on EKE variations and isotropy.

### 6.1. Eddy Kinetic Energy

Altimetric studies of the ocean turbulent eddy field usually assume isotropy. The resulting EKE is then given by the square of the cross-track geostrophic velocity component $U'_c$: EKE = $\langle U'^2_c \rangle$. The suboptimally interpolated gridded maps give us access to both components of the surface current velocity. Thus the EKE (per unit mass) is estimated from the mapped SLA data $\eta'$ by making the assumption of geostrophy only:

$$\mathrm{EKE} = \frac{1}{2}\left[\langle U'^2_g \rangle + \langle V'^2_g \rangle\right],$$

$$U'_g = -\frac{g}{f}\frac{\Delta \eta'}{\Delta y}$$

$$V'_g = \frac{g}{f}\frac{\Delta \eta'}{\Delta x},$$

where $U'_g$ and $V'_g$ denote the zonal and meridional geostrophic velocity anomalies (relative to the three-year mean), $f$ is the Coriolis parameter, $x$ and $y$ are the distances in longitude and latitude, respectively (chosen at 30 km), and $\langle\ \rangle$ denotes the time average.

Plate 8 shows the global EKE distribution from the full resolution combined maps. Sea level gradients along the north Australian coast, and particularly between Papua New Guinea and Australia, are contaminated by residual tidal errors that explain the erroneous value of geostrophic velocities in this area (F. Lyard, personal communication, 1999). As expected, the maximum levels of EKE are concentrated in the vicinity of the major current systems and can reach values of up to 4500 $cm^2\ s^{-2}$ (Plate 8a). The largest value is in the Agulhas region,

with secondary maxima in the Kuroshio, the Gulf Stream, the Brazil/Malvinas Confluence zone, and finally, the Antarctic Circumpolar Current. The combined map shows a very detailed spatial resolution, note, for example, the Subtropical Countercurrent in the northwestern Pacific Ocean, which is a high variable zonal band around 20°N, extending from 130°E to 170°W, previously discussed by *Qiu* [1999]. *Stammer* [1997, Figure 2] finds EKE as high as 3000 $cm^2 s^{-2}$ in the Gulf Stream after averaging T/P along-track data in 2° by 2° geographical boxes. We performed the same spatial averaging on Plate 8 and mapped it again in a log 10 form (as by *Stammer* [1997]). The overall agreement between the smoothed maps is excellent (not shown). Plate 8b is the same as Plate 8a but with EKE values ranging from 0 to 300 $cm^2 s^{-2}$. This change of color scale saturates the well-known high energetic areas and allows us to concentrate on lower EKE regions, over the whole ocean, and to describe their levels and location more precisely. It also enables us to characterize the background noise variance on the EKE field, which is only of the order of 15 $cm^2 s^{-2}$. The low-variability region of the northeastern part of the Pacific Ocean shows spatially nonhomogeneous low values, the lowest values being found south of the Alaskan gyre, centered at 50°N and 150°W, where the EKE is probably underestimated as was found in the North Atlantic subpolar gyre. Similar levels are found in the northern part of the South Atlantic Ocean, which give us a better insight into the lowest EKE levels that can be detected from satellite altimetric data.

Among the many features clearly represented in the North Pacific Ocean are the Oyashio Current, flowing southwestward from the Bering Sea, with a maximum eddy energy level of 400 $cm^2 s^{-2}$ in the vicinity of 45°N and 155°E, and the Alaskan gyre, in the Gulf of Alaska, with maximum EKE of more than 300 $cm^2 s^{-2}$ close to the Aleutian Islands (near 50°N, 170°W). The California Current, between 25° and 45°N, shows a maximum eddy energy level of 250 $cm^2 s^{-2}$ near 125°W, in excellent agreement with results of *Strub et al.* [1997].

In the North Atlantic Ocean the main variable oceanic features are also clearly present in this data set. In particular, the eastward deflection of the North Atlantic Current (NAC), north of Flemish Cap near 50°N, which then splits into two branches flowing northeastward on both the eastern and western flanks of the Rockall Plateau, is associated with high EKE (see *Heywood et al.* [1994], who give a rather exhaustive description of the EKE spatial distribution in the North Atlantic subpolar gyre). Higher EKE are also present near the beginning of the Norway current, at approximately 60°N, 5°W, as it passes northward through the Faeroe-Shetland Channel. The Irminger Current, flowing northeastward along the western flank of the Reykjanes ridge and then veering cyclonically to the southwest along east Greenland, exhibits EKE levels of ~80 $cm^2 s^{-2}$. The so-called North Icelandic Irminger Current, flowing eastward along the northern coast of Iceland, is also well identified. The location where the Irminger Current joins the East Greenland Current, near 65°N, 30°W, displays energy levels of up to 400 $cm^2 s^{-2}$. EKE values of up to 150 $cm^2 s^{-2}$ are also found in the subpolar gyre, at ~60°–62°N and west of 50°W, where the West Greenland Current separates from the coast, and generates eddies. Features like the Labrador Current or the East Greenland Current are barely present on the EKE map since both are more stable currents, essentially controlled by topography. A numerical simulation of their mean kinetic energy shows values of more than 200 $cm^2 s^{-2}$, more than twice the simulated EKE on these maps [cf. *Smith et al.*, 2000, Figures 17a and 17b]. Nevertheless, the Labrador Current can be identified in Plate 8b, as it follows the eastern slope of the Grand Banks, by EKE values around 50 $cm^2 s^{-2}$. In contrast, the Azores front, flowing along 33°N, is well observed by the combined maps with energy ranges from more than 300 $cm^2 s^{-2}$ at 40°W to 150 $cm^2 s^{-2}$ at 20°W.

In the interior of the subtropical gyre of the South Atlantic a zonal band of somewhat higher variability, with EKE values of up to 150 $cm^2 s^{-2}$, extends across the entire gyre at ~33°S. This ocean signal, also present in Plate 4b, corresponds to a rms SLA variability of up to 10 cm and is an oceanic feature, which to our knowledge has not previously been discussed in the literature. It may be related to Rossby wave propagation at the semiannual period [*Le Traon and Minster*, 1993], or at lower frequencies [*Witter and Gordon*, 1999].

In the western Mediterranean, significant EKE values of more than 300 $cm^2 s^{-2}$ are found in the Strait of Gibraltar (36°N, 3°W) corresponding to the temporal variations of the Alboran gyres. Farther East, the Algerian Current eddies, with an EKE level of up to 300 $cm^2 s^{-2}$ off the North African coast (37°N, near 5°E), are also detected, as well as the Ierapetra gyre (35°N, 27°E) [see, e.g., *Ayoub et al.*, 1998]. Even the highly variable Batumi eddy, the main feature of the upper layer variability of the Black Sea circulation can be observed, represented by the small blue spot in the extreme eastern part of the basin [see, e.g., *Oguz et al.*, 1993].

### 6.2. Isotropy and Reynolds Stresses

A first check of ocean isotropy can be obtained through the ratio of the zonal over the meridional geostrophic velocity variances, $I = \langle U_g'^2 \rangle / \langle V_g'^2 \rangle$, and its value as compared to unity. Note that however, $\langle U_g'^2 \rangle = \langle V_g'^2 \rangle$ is not a sufficient condition for isotropy. Nevertheless, it is a first simple way to derive information about the flow field anisotropy, directly from the mapped rms variability. Plate 9 shows the ratio $I$ after averaging of $\langle U_g'^2 \rangle$ and $\langle V_g'^2 \rangle$ in 2° by 2° boxes. A more rigorous analysis was also performed, computing the Reynolds stress covariance term, $\langle U_g' V_g' \rangle$, to represent the magnitude and direction of the eddy variability and estimate the principle axes of variance [e.g., *Wilkin and Morrow*, 1994; *Morrow et al.*, 1994]. An anisotropic flow is then represented by an elongated axis, with the principal direction of the velocity variance being aligned with the direction of the major axis. We computed the ratio of the major over the minor axis amplitudes of the global Reynolds stresses, after spatial averaging in 2° by 2° boxes. The result, not shown here, is in excellent agreement with Plate 9.

We have determined the 95% confidence interval for the ratio $I$. Following *Bendat and Piersol* [1986, p. 84], the ratio of the sample variances of two random variables follows a Fisher distribution. Assuming that at least one map in three is independent and that in a 2° by 2° box, there are four independent estimates (according to the zero crossing of the covariance function in space and time), this gives more than 100 degrees of freedom (from 135 maps covering the 5 ERS years). Therefore, following the $F$ distribution table, we have $F_{100,100,0.05} = 1.39$. Thus, if the ratio $I$ is $>1.39$ or $<0.7$, then the zonal and meridional velocity variances are significantly different (with a confidence of 95%), leading to anisotropy. More zonal variability is present in the near-equatorial band around 10°N in the Pacific Ocean, as expected, because of strong zonal currents at these latitudes. In particular, the most impressive feature in Plate 9 is located at 7°–8°N, between 180° and 260°E, corresponding to the Pacific North Equatorial Countercurrent

[see, e.g., *McPhaden*, 1996]. The western part of the Pacific Ocean is dominated by zonal velocities, $\langle U_g'^2 \rangle$ being up to 2 times larger than $\langle V_g'^2 \rangle$, particularly within the Kuroshio Extension area (150°–180°E; 30°–40°N). The eastern part of the basin shows a reverse tendency, where $\langle U_g'^2 \rangle$ can be smaller than 75% of $\langle V_g'^2 \rangle$. Note that in this region, current velocities are usually much smaller, so that EKE comparisons are less significant than in high-variability areas. No such zonal difference between the western and eastern parts of the basin is found in the North Atlantic Ocean. In low-variability regions, like the eastern part of the South Pacific Ocean, $\langle V_g'^2 \rangle$ is generally significantly larger than $\langle U_g'^2 \rangle$, which may be the signature of westward propagating Rossby wave signals. At higher latitudes, poleward of 60°, $\langle V_g'^2 \rangle$ is generally larger than $\langle U_g'^2 \rangle$ (e.g., Greenland and Barents Seas, north of Scandinavia, in Plate 9), although this is probably not significant. At these latitudes, indeed, the initial grid is strongly anisotropic, and our cubic spline interpolation (see section 4.3.2) cannot totally remove the large difference between zonal and meridional grid spacing distances.

### 6.3. Seasonal Variability

In this section, we use the whole $5\frac{1}{2}$ year period of gridded maps of $\langle U_g'^2 \rangle$ and $\langle V_g'^2 \rangle$ for both T/P and ERS, including the 1997–1998 El Niño warm event. Here we focus on seasonal variability of the EKE field. By investigating time variations of eddy energy one expects to gain insight on how it is generated. In regions of intense currents the main forcing mechanism is generally believed to be the instability processes (barotropic and/or baroclinic) of the mean currents [see, e.g., *Qiu*, 1999]. Note that these changes in eddy energy may indirectly result from external surface forcing like wind or buoyancy effects. In a few areas of low eddy variability, fluctuating wind stress forcing may play an important role in the time evolution of the eddy variability [*White and Heywood*, 1995; *Stammer and Wunsch*, 1999]. In these areas the well-pronounced seasonal cycle present in the external atmospheric forcing fields can be directly responsible for seasonal changes in the eddy variability itself.

Our goal here is mainly descriptive, and we will compare the results with previous studies. Theoretical discussion is beyond the scope of this paper and would be best done by using both altimeter data and high-resolution global circulation modeling results.

To infer a seasonal cycle in the EKE field, we first computed EKE monthly values averaged over 1° by 1° bins and 3 months (the month of March, for example, is the mean of February, March, and April). Then a linear trend as well as the mean were removed from the time series at each grid point, and an annual sine was least squares fitted to extract the annual harmonic of the signal period. Note that this analysis would be complete if the seasonal signal were a purely periodic phenomenon. However, annual changes in the EKE field are expected to be more complex than could be described by a single sinusoid, as previously discussed by *Stammer and Wunsch* [1999]. The spatial distribution of the amplitude and the phase of the annual harmonic is shown in Plates 10a and 10b, respectively. The percentage of the variance in the detrended EKE time series explained by the annual harmonic is shown in Plate 10c. To be able to identify large-scale features, a Loess smoother [*Schlax and Chelton*, 1992] was applied to the three maps, with cutoff wavelengths of 5° in both latitude and longitude.

The largest amplitudes, of more than 400 $cm^2\ s^{-2}$, are found in the Gulf Stream and the Kuroshio Current systems, as well as in the Antarctic Circumpolar Current, but most of the seasonal changes there are below 20% of the EKE variance over the whole period. Also note that in these regions, *Stammer and Wunsch* [1999, Figure 9] find maximum amplitudes of up to 200 $cm^2\ s^{-2}$, a factor of 2 less than in our analysis, which is likely due to smoothing effects. There are, however, very pronounced seasonal cycles in other areas that we review here, basin by basin.

**6.3.1. Atlantic Ocean.** The North Equatorial Counter Current (NECC) exhibits an amplitude of the annual harmonic of up to 400 $cm^2\ s^{-2}$, explaining up to 60% of the EKE variance. Maximum amplitudes are found in October/November, when the retroflection of the North Brazil Current (NBC) into the NECC is well developed [*Johns et al.*, 1998; *Larnicol*, 1998].

In the eastern Caribbean Sea, EKE seasonal variations show amplitudes of the order of 200 $cm^2\ s^{-2}$ that explain up to 60% of the EKE variance with the maximum occurring in April/May. This lags by 2–3 months the maximum in the seasonal variations of the EKE field near 8°N, 50°W found by *Didden and Schott* [1993, see Figure 8b], which is consistent with the 2 months needed by eddies to propagate along the north Brazil coast between 50° and 60°W. This is also in good agreement with *Carton and Chao*'s [1999] results and likely due to annual fluctuations in the trade winds [*Nystuen and Andrade*, 1993]. Note again that this well-defined feature is also absent from *Stammer and Wunsch*'s [1999] map.

Farther north, the northeastern part of the basin, south of Iceland, as well as the Labrador Sea present small annual cycles with amplitudes of the order of 40–50 $cm^2\ s^{-2}$, which explain up to 60% of the EKE variance. Maximum values of EKE are found in April/May in both regions and correspond to regions where a significant correlation with wind stress and wind stress curl was previously found [*White and Heywood*, 1995; *Stammer and Wunsch*, 1999].

**6.3.2. Pacific Ocean.** Regions of enhanced amplitudes of up to 200 $cm^2\ s^{-2}$ are found in the Subtropical Countercurrent (STCC, 19°–25°N; 135°E–175°W) that explain up to 60% of the EKE variance over the whole combined period. The maximum EKE peak is found in June/July. This result is in excellent agreement with *Qiu*'s [1999] results, which show that it is due to the strong seasonality of the two conditions favorable for baroclinic instability: both the strong vertical shear of the STCC/North Equatorial Current (NEC) system and the low-density difference between the STCC and NEC layers. Again, the signal in the STCC, near 20°N, is absent from *Stammer and Wunsch* [1999, Figure 9c]. Plate 11 shows the monthly mean time series for the EKE as well as both the zonal $\langle U_g'^2 \rangle$ and meridional $\langle V_g'^2 \rangle$ components of the velocity variance. If the large surface velocity variance were only due to the seasonal fluctuations of the eastward flowing STCC, we might expect $\langle U_g'^2 \rangle$ to be systematically higher than $\langle V_g'^2 \rangle$. However, one observes that $\langle V_g'^2 \rangle$ is almost always slightly stronger than $\langle U_g'^2 \rangle$ (up to 35% in 1993). This means that the EKE variability in the STCC is mainly due to mesoscale eddy signals, which overwhelm changes in the STCC, as already noted by *Qiu* [1999]. This example clearly shows the interest of having both components of the geostrophic velocity, which has not been possible so far with along-track data, to understand further the EKE sources, whether EKE is due to fluctuations of the mean current or eddy variability.

In the northern part of the basin, small seasonal amplitudes

of ~50 $cm^2 s^{-2}$ explain up to 60% of the total EKE variance of the detrended time series. Maximum EKE occurs in October/November and likely corresponds to the annual cycle of the wind stress [*Stammer and Wunsch*, 1999, Figure 18]. Also, note the maximum annual amplitudes of up to 80 $cm^2 s^{-2}$ in the California Current occurring in June/July near the coast and later offshore in August/September, where they explain up to 60% of the total variance. This has previously been discussed and tentatively associated with baroclinic instability of the southward California Current, which seasonally migrates offshore [*Strub et al.*, 1987; *Kelly et al.*, 1998]. In the central equatorial Pacific Ocean, amplitudes of up to 100 $cm^2 s^{-2}$ near 10°N are likely related to the NECC and account for up to 40% of the EKE variance.

At last a zonal band with enhanced seasonal amplitudes of more than 100 $cm^2 s^{-2}$ that explain up to 60% of the EKE variance is found in the northern part of the western South Pacific, near 15°S, where EKE peak values occur in October/November. This is consistent with *Morris et al.*'s [1996] results, which showed a prominent annual intensification of the gyre-scale circulation in the subtropical South Pacific Ocean with a maximum in November, possibly forced by seasonal wind forcing.

**6.3.3. Indian Ocean.** In the Arabian Sea the amplitude of the annual harmonic reaches 100 $cm^2 s^{-2}$, where it explains up to 60% of the total EKE variance. The maximum EKE is found in winter and is likely due to intense, annually reversing monsoonal winds, and the associated reversal of the ocean surface circulation (see *Kumar and Prasad* [1999] for a review). Near 8°N in the west and along the horn of Africa, where the Great whirl is seasonally present, the annual amplitude reaches 800 $cm^2 s^{-2}$, explaining more than 70% of the total variance. This is in qualitative agreement with the analysis of *Perigaud and Minster* [1988] from Seasat altimeter data, who show strong surface topography amplitudes variations (more than 30 cm in 15 days), north of 5°N. This anticyclonic gyre, observed during the summer monsoon, starts propagating northeastward, at up to 1 m $s^{-1}$ during August/September [*Schott and Quadfasel*, 1982], when the maximum EKE occurs (Plate 10b), before weakening and collapsing at the end of the summer monsoon.

Farther east, annual amplitudes in the western boundary current of the Bay of Bengal reach more than 300 $cm^2 s^{-2}$ with a maximum in April/May and account for up to 50% of the total variance. This corresponds well with the seasonal cycle of the current discussed by *Shetye et al.* [1993], who propose that this current is part of a seasonal anticyclonic subtropical gyre, which is best developed in March/April as a response to the wind stress curl over the bay.

In the northern part of the South Indian Ocean an almost zonal band between 10° and 30°S, from offshore the northeastern edge of Madagascar (near 10°S, 70°E) to the southwestern corner of Australia (30°S, 110°E), shows an annual harmonic with amplitudes as large as 300 $cm^2 s^{-2}$ accounting for up to 60% of the total variance. This annual harmonic is large in three different areas that could correspond to three distinct eddy generation seasonal mechanisms.

1. Near 30°S, 110°E the annual harmonic reaches amplitudes near 300 $cm^2 s^{-2}$, which explain up to 60% of the total EKE variance. The maximum is found in June/July, which corresponds to the time of maximum strength of the southward Leeuwin Current seaward of the shelf edge [*Smith et al.*, 1991] and might thus correspond to baroclinic instabilities of the current [see also *Morrow and Birol*, 1998].

2. North of that region, between roughly 10°–20°S, 90°–120°E, amplitudes of the order of 100 $cm^2 s^{-2}$ reach their maximum in October and explain from 30 to 60% of the total variance. In this region the annual signal in the EKE field could correspond to the seasonally varying instabilities associated with westward and northward propagation of annual Rossby waves that travel across the basin [*Perigaud and Delecluse*, 1992; *Morrow and Birol*, 1998]. Whether these waves are triggered by the fluctuations in the Indonesian Throughflow and/or by the seasonal cycle in the wind stress curl east of 100°E is still a matter of debate [*Birol and Morrow*, 2000].

3. In the western part of the basin, between 10°–15°S and 50°–80°E, amplitudes of up to 150 $cm^2 s^{-2}$ (at 65°E, 15°S) account for up to 60% of the total EKE variance. The maximum of the seasonal variations occurs in January, in phase with what is observed in the Arabian Sea. This area could thus be directly forced by the seasonal reversal of the monsoonal winds.

## 7. Conclusion

Using altimeter data from the first $5\frac{1}{2}$ years of T/P and ERS-1 and -2 35 day repeat cycle data, we have shown the contribution of their merging to mesoscale ocean studies. The intercalibrated and homogeneous gridded data sets have an excellent global compatibility, the rms of their differences being less than 3 cm in low ocean variability regions. In high-variability areas the differences are mainly explained by the mapping errors. The mapping of the ocean signal was done globally through an improved objective analysis method that takes long wavelength residual errors into account and uses realistic correlation scales of the ocean circulation (e.g., 175 km at 30°N/°S and 100 km at 60°N/°S), with a global high-resolution of 1/4°. The combination also significantly homogenizes and reduces the mapping error. A statistical description, based on the comparison between T/P-only maps and the merged ones, was used to demonstrate the contribution of the combination for further mesocale investigations. We confirm that if one wants to consider realistic correlation scales of the ocean dynamics, T/P data are not sufficient on their own owing to the too large spatial sampling of the satellite tracks. So, with our choice of realistic decorrelation scales, unrealistic features appear in the high-variability areas on the T/P rms SLA variability map, which disappear on the combined map. As far as geostrophic velocity calculations are concerned, T/P + ERS data enable us to get a better estimation of the meridional velocity and to observe ~30% more kinetic energy, in both directions, than T/P data alone. Wavenumber spectra were also used to demonstrate that the combination of T/P and ERS data enables us to recover signals with wavelengths >150–200 km in all directions and, in particular, in the zonal one.

A careful comparison with WOCE surface drifters in the North Atlantic as well as with current meters revealed that the combined product captures the spatial structure of the observed variability, except in the subpolar region or close to the shelf breaks, where current variability is underestimated. Compared to the drifter, there is also an unexplained difference with the zonal velocity component $U'_g$ having less variability and the meridional one, $V'_g$, having more in high-energy regions (Gulf Stream). Part of these discrepancies might, however, result from the insufficient sampling of the drifter set and from the nonsimultaneity of both data sets.

A first global analysis of the combined data focused on EKE

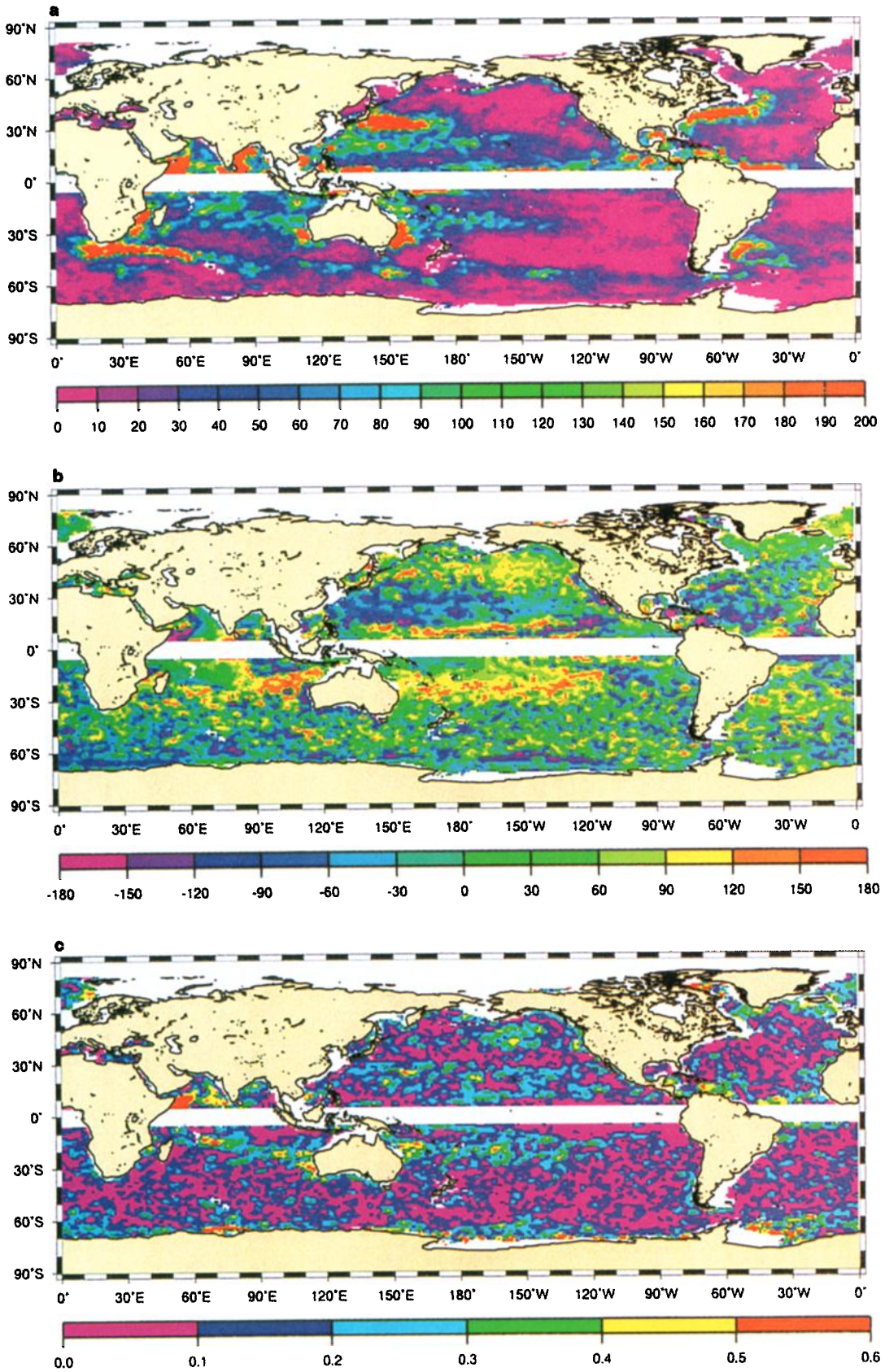


**Plate 10.** Seasonal cycle of EKE estimated from time series of monthly mean EKE: (a) the amplitude in $cm^2$ $s^{-2}$, (b) the phase in degrees relative to November, and (c) the explained percentage of the total EKE variance. Only values over water depths >500 m are shown.

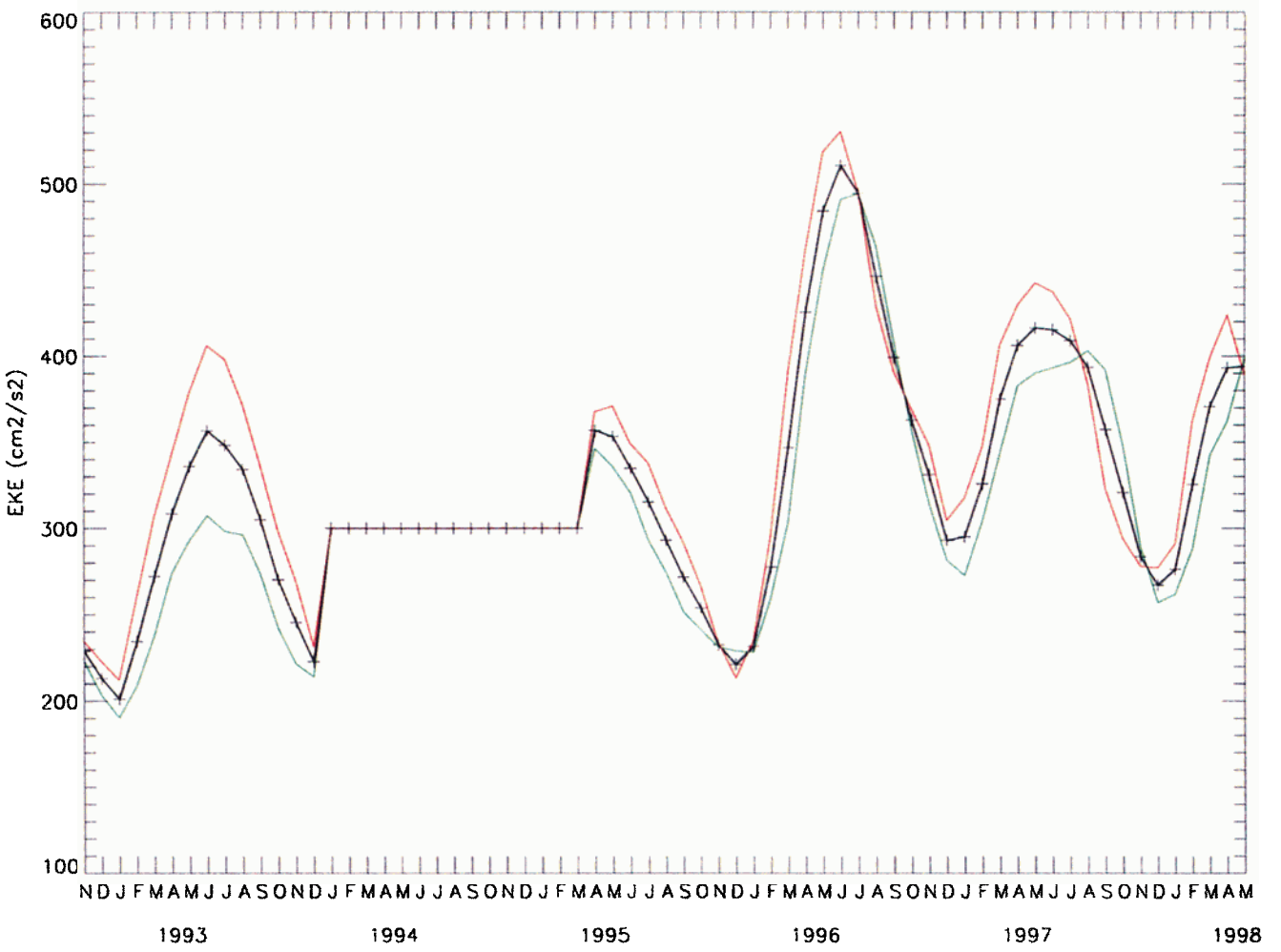


**Plate 11.** Time series of monthly mean EKE inferred from T/P + ERS-1 and -2 maps in the Subtropical Countercurrent region of 19°–25°N, 135°E–175°W. Estimates are given for EKE (black), $\langle U_g'^2 \rangle$ (green), and $\langle V_g'^2 \rangle$ (red). Estimates are given from November 1992 to May 1998 and smoothed by a 3 month running mean (see text).

variations and isotropy. The very high resolution obtained with the merged data, never previously achieved so far at a global scale, enabled a detailed description of the mesoscale surface variability. The background noise level in the EKE field was found to be of the order of 15 $cm^2\ s^{-2}$, with minimum values found in the northeastern part of the North Pacific Ocean and the northern part of the South Atlantic Ocean. The ratio of $\langle U_g'^2 \rangle$ over $\langle V_g'^2 \rangle$ over the global ocean revealed significant differences between the North Atlantic and Pacific Oceans. Whereas the eddy velocity field in the Atlantic was found to be rather isotropic, it is dominated by zonal (meridional) velocities in the western (eastern) part of the Pacific. A detailed review of the locations in the world ocean where the annual harmonic explains a significant part of the EKE variance was discussed, referring to previous studies. The interest of having access to both components of the geostrophic velocity was also highlighted in the STCC, where the mean flow variations were shown to be dominated by eddy-like variability.

A more detailed analysis of these regional features, as well as an attempt to get insight into the physical mechanisms leading to some of the observed seasonal variations in EKE, is beyond the scope of this paper and will be part of a regional study. This will allow us to describe further regional oceanographic features as well as to get a much finer insight into local anisotropy.

## Appendix: Mapping Methodology

The method is a global suboptimal space-time objective analysis, which takes into account along-track correlated errors. Expressions for the best least squares linear estimator $\theta_{est}(x)$ and the associated error field are recalled here [*Bretherton et al.*, 1976]:

$$\theta_{est}(x) = \sum_{i=1}^{n} \sum_{j=1}^{n} A_{ij}^{-1} C_{xj} \Phi_{obs'}, \tag{1}$$

with $\Phi_{obs'} = \Phi_i + \varepsilon_i$, $\Phi_i$ being the true value of the SLA and $\varepsilon_i$ being the measurement error. $A$ is the covariance matrix of the observations themselves, and $C$ is the covariance vector of the observations and the field to be estimated:

$$A_{ij} = \langle \Phi_{obs'} \Phi_{obs'} \rangle = \langle \Phi_i \Phi_j \rangle + \langle \varepsilon_i \varepsilon_j \rangle$$

$$C_{xi} = \langle \theta(x) \Phi_{obs'} \rangle = \langle \theta(x) \Phi_i \rangle.$$

The associated error variance $e^2$ is given by

$$e^2 = C_{xx} - \sum_{i=1}^{n} \sum_{j=1}^{n} C_{xi} C_{xj} A_{ij}^{-1}. \quad (2)$$

To take account of the correlated long wavelength errors, $\langle \varepsilon_i \varepsilon_j \rangle$ is expressed in the following form:

$\langle \varepsilon_i \varepsilon_j \rangle = \delta_{i,j} b^2$ for points $i, j$ not on the same track

or in the same cycle

$\langle \varepsilon_i \varepsilon_j \rangle = \delta_{i,j} b^2 + E_{LW}$ for points $i, j$ on the same track

and in the same cycle,

where $b^2$ and $E_{LW}$ are the variances of the white measurement noise and of the long wavelength error, respectively.

The following space-time correlation function $C(r, t)$ is used [*Arhan and Colin de Verdière*, 1985]:

$$C(r, t) = [1 + ar + 1/6(ar)^2 - 1/6(ar)^3] \cdot \exp(-ar) \exp(-t^2/T^2),$$

where $r$ is distance, $t$ is time, $L = 3.34/a$ is the first zero crossing of $C$, and $T$ is the $e$-folding time. $T$ is set at 10 days at the equator between 5°S and 5°N and at 15 days outside this equatorial band (see text).

To reduce computer time needed to select data and invert the covariance matrix $A$, the objective analysis (data selection, matrix $A$ inversion, and estimate and error calculations) is performed on a coarse-resolution grid of 1° by 1° spacing. Each 1° main grid point is then associated with the fifteen closest 0.25° subgrid points. The same data set and the same matrix $A$ are used to compute the estimates and mapping errors of the 1/4 grid points. In order that all grid points are estimated with a number of observations at least corresponding to the zero crossing of the correlation function we select the radius of the subdomain associated with the main grid point to be the zero crossing of the space correlation function extended by 0.5°. Each combined T/P + ERS-1 and -2 global 0.25° map took about 6 CPU hours on an SGI Power Challenge 194 MHz R10000 processor, equivalent to 180 Mflops.

**Acknowledgments.** We are especially grateful to Rosemary Morrow for her careful reading of the manuscript and her comments, which were very helpful. We also thank the reviewers for their detailed comments, which led to a much improved and more readable manuscript. The objective analysis code was run on a Silicon Graphics Power Challenge at CERFACS (European Center for Research and Advanced Training in Scientific Computation), based in Toulouse (France), which allowed us to save much CPU time. This work was realized as part of the Environment and Climate EU AGORA (ENV4-CT9560113) and DUACS (ENV44-T96-0357) projects. The merged maps are available through AVISO (http://www-aviso.cls.cnes.fr). The WOCE drifter data were communicated by the WOCE drifter data assembly center at AOML (NOAA) in Miami.

## References

Archiving, Validation, and Interpretation of Satellite Oceanographic Data (AVISO), *AVISO Handbook for Merged TOPEX/Poseidon Products*, 3rd ed., Toulouse, France, 1996.

Arhan, M., and A. Colin de Verdière, Dynamics of eddy motions in the eastern North Atlantic, *J. Phys. Oceanogr.*, *15*, 153–170, 1985.

Ayoub, N., P.-Y. Le Traon, and P. De Mey, A description of the Mediterranean surface variable circulation from combined ERS-1 and TOPEX/Poseidon altimetric data, *J. Mar. Sys.*, *18*, 3–40, 1998.

Bendat, J. S., and A. G. Piersol, Random Data: Analysis and measurement procedures (second edition), edited by J. Wiley & Sons, pp. 566, Wiley Interscience, 1986.

Birol, F., and R. Morrow, Source of the baroclinic waves in the southeast Indian, *J. Geophys. Res.*, in press, 2000.

Blayo, E., T. Mailly, B. Barnier, P. Brasseur, C. Le Provost, J. M. Molines, and J. Verron, Complementarity of ERS-1 and TOPEX/Poseidon altimeter data in estimating the ocean circulation: Assimilation into a model of the North Atlantic, *J. Geophys. Res.*, *102*, 18,573–18,584, 1997.

Bretherton, F., R. Davis, and C. Fandry, A technique for objective analysis and design of oceanographic experiments applied to MODE-73, *Deep Sea Res. Oceanogr. Abstr.*, *23*, 559–582, 1976.

Brink, N. J., K. A. Moyer, R. P. Trask, and R. A. Weller, The Subduction Experiment: Mooring field program and data summary, *Tech. Rep. WHOI-95-08*, Woods Hole Oceanogr. Inst., Woods Hole, Mass., 1995.

Brügge, B., Near-surface mean circulation and kinetic energy in the central North Atlantic from drifter data, *J. Geophys. Res.*, *100*, 20,543–20,554, 1995.

Carton, J. A., and Y. Chao, Caribbean Sea eddies inferred from TOPEX/Poseidon altimetry and a 1/6° Atlantic Ocean model simulation, *J. Geophys. Res.*, *104*, 7743–7752, 1999.

Centre ERS d'Archivage et de Traitement (CERSAT), *ERS-1 Altimeter Products User Manual*, Brest, France, 1994.

Centre ERS d'Archivage et de Traitement (CERSAT), *Altimeter and Microwave Radiometer ERS Products User Manual*, Brest, France, 1996.

Chao, S.-Y., and L.-L. Fu, Comparison between the TOPEX/Poseidon data and a global ocean general circulation model during 1992–1993, *J. Geophys. Res.*, *100*, 24,965–24,976, 1995.

Deque, M., C. Dreveton, A. Braun, and D. Cariolle, The ARPEGE/IFS atmosphere model: A contribution to the French community climate modelling, *Clim. Dyn.*, *10*, 249–266, 1994.

Didden, N., and F. Schott, Eddies in the North Brazil current retroflection region observed by Geosat altimetry, *J. Geophys. Res.*, *98*, 20,121–20,131, 1993.

Eymard, L., et al., Study of the air-sea interactions at the mesoscale: The SEMAPHORE experiment, *Ann. Geophys.*, *14*, 986–1015, 1996.

Fukumori, I., Assimilation of TOPEX sea level measurements with a reduced-gravity, shallow water model of the tropical Pacific Ocean, *J. Geophys. Res.*, *100*, 25,027–25,039, 1995.

Greenslade, D. J. M., D. B. Chelton, and M. G. Schlax, The midlatitude resolution capability of sea level fields constructed from single and multiple satellite altimeter datasets, *J. Atmos. Oceanic Technol.*, *14*, 849–870, 1997.

Hamming, R. W., *Digital Filters*, *Prentice-Hall Signal Proc. Ser.*, edited by A. V. Oppenheim Prentice-Hall, Englewood Cliffs, N. J., 1977.

Hansen, D. V., and P.-M. Poulain, Quality control and interpolations of WOCE/TOGA drifter data, *J. Atmos. Oceanic Technol.*, *13*, 900–909, 1996.

Hernandez, F., P.-Y. Le Traon, and R. Morrow, Mapping mesoscale variability of the Azores current using TOPEX/Poseidon and ERS-1 altimetry, together with hydrographic and Lagrangian measurements, *J. Geophys. Res.*, *100*, 24,995–25,006, 1995.

Heywood, K. J., E. L. McDonagh, and M. A. White, Eddy kinetic energy in the North Atlantic subpolar gyre from satellite altimetry, *J. Geophys. Res.*, *99*, 22,525–22,539, 1994.

Johns, W. E., T. N. Lee, R. C. Beardsley, J. Candela, R. Limeburner, and B. Castro, Annual cycle and variability of the North Brazil Current, *J. Phys. Oceanogr.*, *28*, 103–128, 1998.

Kelly, K. A., R. C. Beardsley, R. Limeburger, K. H. Brink, J. D. Paduan, and T. K. Chereskin, Variability of the near-surface eddy kinetic energy in the California Current based on altimetric, drifter, and moored current data, *J. Geophys. Res.*, *103*, 13,067–13,083, 1998.

Koblinsky, C. J., P. Gaspar, and G. Lagerloef, The future of spaceborn altimetry: Ocean and climate change, report, 75 pp., Joint. Oceanogr. Inst. Inc., Washington, D. C., 1992.

Kumar, S. P., and T. G. Prasad, Formation and spreading of Arabian sea high-salinity water mass, *J. Geophys. Res.*, *104*, 1455–1464, 1999.

Larnicol, G., Analyse de la Variabilité de l'Océan Atlantique à Partir des Données Altimétriques TOPEX/Poseidon et d'un Modèle Inverse non Linéaire, Ph.D. thesis, Univ. de Bretagne Occidentale, Brest, France, 1998.

Le Traon, P.-Y., and G. Dibarboure, Mesoscale mapping capabilities of multiple-satellite altimeter missions, *J. Atmos. Oceanic Technol.*, *16*, 1208–1223, 1999.

Le Traon, P.-Y., and J.-F. Minster, Sea level variability and semiannual Rossby waves in the South Atlantic subtropical gyre, *J. Geophys. Res.*, *98*, 12,315–12,326, 1993.

Le Traon, P.-Y., and F. Ogor, ERS-1/2 orbit improvement using TOPEX/Poseidon: The 2 cm challenge, *J. Geophys. Res.*, *103*, 8045–8057, 1998.

Le Traon, P.-Y., P. Gaspar, F. Ogor, and J. Dorandeu, Satellites work in tandem to improve accuracy of data, *Eos Trans. AGU*, *76*, 385–389, 1995.

Le Traon, P.-Y., F. Nadal, and N. Ducet, An improved mapping method of multi-satellite altimeter data, *J. Atmos. Oceanic Technol.*, *15*, 522–534, 1998.

McPhaden, M. J., Monthly period oscillations in the Pacific North Equatorial Countercurrent, *J. Geophys. Res.*, *101*, 6337–6359, 1996.

Morris, M., D. Roemmich, and B. Cornuelle, Observations of variability in the South Pacific subtropical gyre, *J. Phys. Oceanogr.*, *26*, 2359–2380, 1996.

Morrow, R., and F. Birol, Variability in the southeast Indian Ocean from altimetry: Forcing mechanisms for the Leeuwin Current, *J. Geophys. Res.*, *103*, 18,529–18,544, 1998.

Morrow, R., R. Coleman, J. Church, and D. Chelton, Surface eddy momentum flux and velocity variances in the Southern Ocean from Geosat altimetry, *J. Phys. Oceanogr.*, *24*, 2050–2071, 1994.

Niiler, P. P., R. E. Davis, and H. J. White, Water-following characteristics of a mixed layer drifter, *Deep Sea Res., Part A*, *31*, 1867–1881, 1987.

Niiler, P. P., A. S. Sybrandy, K. Bi, P.-M. Poulain, and D. Bitterman, Measurements of the water-following capability of holey-sock and TRISTAR drifters, *Deep Sea Res., I*, *42*, 1951–1964, 1995.

Nystuen, J. A., and C. A. Andrade, Tracking mesoscale ocean features in the Caribbean Sea using Geosat altimetry, *J. Geophys. Res.*, *98*, 8389–8394, 1993.

Oguz, T., V. S. Latun, M. A. Latif, V. V. Vladimirov, H. I. Sur, A. A. Markov, E. Özsoy, B. B. Kotovshchikov, V. V. Eremeev, and Ü. Ünlüata, Circulation in the surface and intermediate layers of the Black Sea, *Deep Sea. Res., I*, *40*, 1597–1612, 1993.

Oschlies, A., and J. Willebrand, Assimilation of Geosat altimeter data into an eddy-resolving primitive equation model of the North Atlantic Ocean, *J. Geophys. Res.*, *101*, 14,175–14,190, 1996.

Perigaud, C., and P. Delecluse, Annual sea level variations in the southern tropical Indian Ocean from Geosat and shallow-water simulations, *J. Geophys. Res.*, *97*, 20,169–20,178, 1992.

Perigaud, C., and J.-F. Minster, Variability of the Somali Current as observed from Seasat altimetry, *J. Phys. Oceanogr.*, *18*, 25–39, 1988.

Picaut, J., A. J. Busalacchi, M. J. McPhaden, and B. Camusat, Validation of the geostrophic method for estimating zonal currents at the equator from Geosat altimeter data, *J. Geophys. Res.*, *95*, 3015–3024, 1990.

Qiu, B., Seasonal eddy field modulation of the North Pacific Subtropical Coutercurrent: TOPEX/Poseidon observations and theory, *J. Phys. Oceanogr.*, *29*, 2471–2486, 1999.

Richardson, P. L., Eddy kinetic energy in the North Atlantic from surface drifters, *J. Geophys. Res.*, *88*, 4355–4367, 1983.

Schlax, M. G., and D. B. Chelton, Frequency domain diagnostics for linear smoothers, *JASA J. Am. Stat. Assoc.*, *87*, 1070–1081, 1992.

Schott, F., and D. Quadfasel, Variability of the Somali current system during the onset of the southwest monsoon, *J. Phys. Oceanogr.*, *12*, 1343–1357, 1982.

Shetye, S. R., A. D. Gouveia, S. S. C. Shenoi, D. Sundar, G. S. Michael, and G. Nampoothiri, The western boundary current of the seasonal subtropical gyre in the Bay of Bengal, *J. Geophys. Res.*, *98*, 945–954, 1993.

Smith, R. D., M. E. Maltrud, F. O. Bryan, and M. W. Hecht, Numerical simulation of the North Atlantic Ocean at 1/10°, *J. Phys. Oceanogr.*, *30*, 1532–1561, 2000.

Smith, R. L., A. Huyer, J. S. Godfrey, and J. A. Church, The Leeuwin current off western Australia, 1986–1987, *J. Phys. Oceanogr.*, *21*, 323–345, 1991.

Stammer, D., Global characteristics of ocean variability estimated from regional TOPEX/Poseidon altimeter measurements, *J. Phys. Oceanogr.*, *27*, 1743–1769, 1997.

Stammer, D., and C. Wunsch, Temporal changes in eddy energy of the oceans, *Deep Sea Res., II*, *46*, 77–108, 1999.

Stammer, D., C. Wunsch, and R. M. Ponte, De-aliasing of global high frequency barotropic motions in altimeter observations, *Geophys. Res. Lett.*, *27*, 1175–1178, 2000.

Strub, P. T., J. S. Allen, A. Huyer, R. L. Smith, and R. C. Beardsley, Seasonal cycle of currents, temperatures, winds, and sea level over the northeast Pacific continental shelf: 35°N to 48°N, *J. Geophys. Res.*, *92*, 1507–1526, 1987.

Strub, P. T., T. K. Chereskin, P. P. Niiler, C. James, and M. D. Levine, Altimeter-derived variability of surface velocities in the California Current System, 1, Evaluation of TOPEX altimeter velocity resolution, *J. Geophys. Res.*, *102*, 12,727–12,748, 1997.

Tierney, C., J. Wahr, F. Bryan, and V. Zlotnicki, Short-period oceanic circulation: Implications for satellite altimetry, *Geophys. Res. Lett.*, *27*, 1255–1258, 2000.

Tychensky, A., P.-Y. Le Traon, F. Hernandez, and D. Jourdan, Large structures and temporal change in the Azores front during the Semaphore experiment, *J. Geophys. Res.*, *103*, 25,009–25,027, 1998.

Van Meurs, P., and P. P. Niiler, Temporal variability of the large scale geostrophic surface velocity in the northeast Pacific, *J. Phys. Oceanogr.*, *27*, 2288–2297, 1997.

White, M. A., and K. Heywood, Seasonal and interannual changes in the North Atlantic subpolar gyre from Geosat and TOPEX/Poseidon altimetry, *J. Geophys. Res.*, *100*, 24,931–24,941, 1995.

Wilkin, J. L., and R. Morrow, Eddy kinetic energy and momentum flux in the Southern Ocean: Comparison of a global eddy-resolving model with altimeter, drifter, and current-meter data, *J. Geophys. Res.*, *99*, 7903–7916, 1994.

Witter, D. L., and A. L. Gordon, Interannual variability of South Atlantic circulation from four years of TOPEX/Poseidon satellite altimeter observations, *J. Geophys. Res.*, *104*, 20,927–20,948, 1999.

Wunsch, C., The vertical partition of oceanic horizontal kinetic energy, *J. Phys. Oceanogr.*, *27*, 1770–1794, 1997.

Zlotnicki, V., G. Siedler, and Birgit Klein, Can the weak surface currents of the Cape Verde frontal zone be measured with altimetry?, *J. Geophys. Res.*, *98*, 2485–2493, 1993.

N. Ducet and P. Y. Le Traon, CLS Space Oceanography Division, 8-10 rue Hermes, 31526 Ramonville Saint-Agne, France. (nicolas.ducet@cls.fr)

G. Reverdin, LEGOS, CNES/GRGS/LEGOS/UMR5566, 18 Avenue Edouard Belin, 31401 Toulouse Cedex 4, France.

(Received May 18, 1999; revised February 14, 2000;
accepted March 20, 2000.)